

# From Single Storms to Large-Scale Waves: A Multi-Year Kilometer-Scale Global Simulation

Andreas F. Prein<sup>1</sup>, Praveen K. Pothapakula<sup>1</sup>, Christian Zeman<sup>1</sup>, Morgane Lalonde<sup>1</sup>, Marius Rixen<sup>1</sup>, Anurag Dipankar<sup>2</sup>, Matthieu Leclair<sup>2</sup>, and Andreas Jocksch<sup>3</sup>

<sup>1</sup>Institute for Atmospheric and Climate Science, ETH Zürich, 8092 Zurich, Switzerland

<sup>2</sup>Center for Climate Systems Modeling (C2SM), ETH Zürich, Zurich, Switzerland

<sup>3</sup>Swiss National Supercomputing Centre (CSCS), ETH Zürich, Lugano, Switzerland

**Correspondence:** Andreas F. Prein (aprein@ethz.ch)

1 **Abstract.** Global kilometer-scale (km-scale) weather and climate models offer new opportunities to unify numerical weather  
2 prediction (NWP) and climate modeling by explicitly simulating convection and mesoscale circulations globally within a single  
3 modeling framework. We present results from the first multi-year (April 2020–March 2024) global atmosphere-land simula-  
4 tion using the GPU-refactored ICON model at a 2.5 km horizontal grid spacing and 120 vertical levels. The simulation uses  
5 NWP physics and observed sea-surface temperatures. We assess its performance against satellite, reanalysis, and in-situ ob-  
6 servations using standard statistics and the MOAAP feature-tracking framework to evaluate a wide spectrum of atmospheric  
7 phenomena. ICON reproduces global temperature and precipitation patterns, including a realistic single Intertropical Con-  
8 vergence Zone and physically consistent diurnal precipitation cycles. However, ICON exhibits continental summertime warm  
9 and dry biases, linked to an overestimation of incoming solar radiation and excessive surface sensible heat fluxes. The model  
10 realistically captures the intensity and frequency of hourly precipitation and near-surface winds, as well as the structure and  
11 occurrence of tropical cyclones. Mesoscale convective systems (MCSs) exhibit realistic spatial initiation patterns, but their  
12 frequency is underestimated over oceans and overestimated over tropical land. Long-lived MCSs are too infrequent and small,  
13 while increased rainfall from shallow and mid-level clouds may reflect overactive warm-cloud microphysics or observational  
14 deficiencies. These biases might stem in part from a misrepresentation of thermodynamic-convection coupling. Our results  
15 demonstrate the feasibility and scientific value of multi-year global km-scale simulations for exploring the weather–climate  
16 system and local-scale extreme events, while identifying key directions for future model development.

## 17 1 Introduction

18 The consequences of anthropogenic climate change are increasingly visible through record-breaking extreme events and their  
19 associated impacts (e.g., Donat et al., 2016; IPCC, 2023; Seneviratne et al., 2021; Perkins-Kirkpatrick and Lewis, 2020).  
20 Reliable, local-scale climate information to support adaptation and mitigation efforts is urgently needed, as many extremes  
21 and their impacts occur at spatial scales that are poorly represented in state-of-the-art global climate models (Giorgi and  
22 Gutowski Jr, 2015; IPCC, 2023). Kilometer-scale (km-scale) weather and climate models, with horizontal grid spacings of a  
23 few kilometers, have emerged as promising tools to bridge this gap by explicitly resolving deep convection, orographic flows,

24 and other mesoscale phenomena (Prein et al., 2015; Kendon et al., 2017; Lucas-Picher et al., 2021). However, the computational  
25 cost of km-scale modeling has historically restricted its use to limited-area domains over relatively small regions. Recent  
26 advances in model development, numerical efficiency, and high-performance computing now enable month- to multi-year-long  
27 km-scale simulations to be conducted globally (Stevens et al., 2019; Schär et al., 2020; World Climate Research Programme,  
28 2022), opening unprecedented opportunities to study mesoscale processes and their interactions with synoptic- and planetary-  
29 scale circulations within a physically consistent framework.

30 Regional km-scale climate modeling has rapidly evolved over the past decade and has now reached a mature stage of sci-  
31 entific and technical development (Prein et al., 2015; Ban et al., 2014; Kendon et al., 2021; Marsham et al., 2013). A central  
32 research focus has been to identify the added value of km-scale simulations compared to coarser, convection-parameterized  
33 models. Numerous studies have demonstrated that the intermittency, intensity, frequency, and phase of precipitation are sub-  
34 stantially improved when deep convection is explicitly resolved (e.g., Holloway et al., 2012; Prein et al., 2013; Ban et al.,  
35 2014; Kendon et al., 2017). In particular, sub-daily precipitation extremes are much better captured (e.g., Ban et al., 2014;  
36 Prein et al., 2015, 2017; Ban et al., 2021; Pichelli et al., 2021) and the diurnal cycle of convective precipitation is more re-  
37 alistically represented (e.g., Sato et al., 2009; Marsham et al., 2013; Ban et al., 2014; Prein et al., 2013). Furthermore, the  
38 spatial organization of convection, including mesoscale convective systems and tropical cyclones, is substantially improved in  
39 km-scale models (e.g., Miura et al., 2007a; Gentry and Lackmann, 2010; Clark et al., 2016; Prein et al., 2020, 2021, 2022;  
40 Gutmann et al., 2018). Consistent with the explicit treatment of deep convection, km-scale simulations also produce convective  
41 wind gusts and straight-line winds that are absent in models with parameterized convection (Prein, 2023; Brown et al., 2024).  
42 Improved representation of topography enhances the simulation of orographic precipitation, mountain snow accumulation, and  
43 valley wind systems (Liu et al., 2017; Ikeda et al., 2021; Schmidli et al., 2018). Additionally, km-scale grids allow for a more  
44 faithful representation of land-atmosphere coupling (Hohenegger et al., 2009; Lee and Hohenegger, 2024; Segura et al., 2022),  
45 and lateral groundwater fluxes can be represented explicitly, which can feed back on soil moisture and precipitation character-  
46 istics (Schlemmer et al., 2018; Barlage et al., 2021). At km-scale resolution, urban areas can be better represented, enabling  
47 more realistic simulations of urban heat islands and their influence on local convection and precipitation (Argüeso et al., 2016;  
48 Langendijk et al., 2021). However, dedicated land surface model development efforts are needed to include processes that are  
49 typically missing (e.g., shallow groundwater flow, urban parameterizations).

50 While many of the mesoscale phenomena examined here have already been studied with regional convection-permitting  
51 models, the added value of the present study is that it evaluates them within a single, consistent, multi-year, global km-scale  
52 framework, enabling direct comparisons across regions and assessments of their links to larger-scale circulation features.

53 The field of global km-scale modeling was pioneered by the Japanese community (Tomita et al., 2005; Miura et al., 2007b;  
54 Satoh et al., 2008) through the development of the Non-hydrostatic ICosahedral Atmospheric Model (NICAM). Over the  
55 last two decades, almost every major model-development center has invested in developing next-generation, non-hydrostatic  
56 global modeling capabilities. At the same time, advances in computer technology made it feasible to run global km-scale  
57 simulations for more than just a few days. The DYAMOND (DYNamics of the Atmospheric general circulation Modeled On  
58 Non-hydrostatic Domains) intercomparison experiments leveraged these developments and initiated the first global, multi-

59 model, km-scale coordinated intercomparison of simulations of the atmosphere at grid spacings of 3 km–5 km (Stevens et al.,  
60 2019; Satoh et al., 2019; Takasuka et al., 2024b). These experiments revealed substantial inter-model differences in the ability  
61 to simulate mesoscale convective systems (MCSs) (Feng et al., 2025) and tropical cyclones (Judt et al., 2021). Some modeling  
62 systems demonstrated notable progress following dedicated model development efforts. For instance, the U.S. Department  
63 of Energy’s SCREAM (Simple Cloud-Resolving E3SM Atmosphere Model) initially underestimated convective organiza-  
64 tion during the first DYAMOND phase but demonstrated marked improvements in MCS and tropical-cyclone structure in  
65 DYAMOND-Winter after major revisions to microphysics and numerics (Taylor et al., 2023; Donahue et al., 2024; Feng et al.,  
66 2025). Beyond convective systems, global km-scale simulations exhibit more realistic representations of equatorial waves and  
67 tropical variability compared to coarser-resolution models (Miura et al., 2007a; Nasuno et al., 2008; Holloway et al., 2012;  
68 Weber and Mass, 2019; Judt and Rios-Berrios, 2021). Ongoing developments extend these atmospheric configurations toward  
69 multidecadal coupled ocean-atmosphere-land models that include interactive ocean, sea ice, and biogeochemical components  
70 (Hohenegger et al., 2023; Segura et al., 2025b; Rackow et al., 2025) as well as the carbon cycle and aerosol emissions (Klocke  
71 et al., 2025).

72 Here, we present an overview of the performance of a global simulation with a 2.5 km horizontal grid spacing spanning  
73 four consecutive years, providing a comprehensive assessment of Earth’s hydroclimate and associated extremes at km-scales.  
74 This simulation represents a major step toward bridging the traditional gap between numerical weather prediction and climate  
75 modeling (Miura et al., 2023; Randall and Emanuel, 2024) by explicitly resolving convective processes and mesoscale storm  
76 systems within a global, multi-year integration. We employ a graphics processing unit (GPU)–refactored version of the ICON  
77 (Icosahedral Nonhydrostatic) model (Zängl et al., 2015; Dipankar et al., 2026) using the physical parameterizations from its  
78 operational Numerical Weather Prediction configuration. Such global storm-resolving simulations provide a unified framework  
79 for studying the dynamics and statistics of phenomena ranging from single storms to global waves, including tropical cyclones,  
80 mesoscale convective systems, and equatorial waves, and for examining their role in shaping large-scale hydroclimatic variabil-  
81 ity and extremes. We use a model setup that is closely aligned with ICON settings used in numerical weather prediction, which  
82 differs substantially in the used physics (i.g, land surface model, surface layer scheme, boundary layer scheme, microphysics,  
83 and radiation) compared to previously performed global km-scale ICON simulations (e.g., Segura et al., 2025a). The primary  
84 objectives of this study are threefold: (i) to document the experimental design and technical aspects of the four-year simula-  
85 tion, (ii) to evaluate its skill in reproducing climate mean states and key mesoscale phenomena and their contribution to global  
86 hydroclimate statistics, and (iii) to identify systematic model deficiencies that can inform future model development. The re-  
87 sulting dataset, which will be openly released through the DYAMOND-III intercomparison initiative (Takasuka et al., 2024b),  
88 provides a novel resource for investigating the physical processes governing the Earth’s hydroclimate in a high-resolution, fully  
89 global context.

## 90 2 Data and Methods

### 91 2.1 Modeling

92 With recent advances in exascale high-performance computing (HPC) architectures, the computational throughput of various  
93 weather and climate models has substantially improved over the last decade. Especially energy-efficient heterogeneous archi-  
94 tectures, leveraging GPU accelerators, have been developed and can make climate model integrations very efficient (Schär  
95 et al., 2020). However, substantial investments in enabling km-scale weather and climate model codes are needed to port them  
96 and run them efficiently on new HPC systems (Giorgetta et al., 2022; Donahue et al., 2024; Dipankar et al., 2026). Rapidly  
97 emerging technologies in hybrid architectures require agile, architecture-agnostic climate model codes. The EXCLAIM (EX-  
98 treme scale Computing and data platform for cLoud-resolving weAther and cIimate Modeling) project at ETH Zürich addresses  
99 this issue by refactoring the ICON code with Domain Specific Language (DSL) with a Python front-end using GridTools for  
100 Python, GT4Py, while enabling backend flexibility across architectures (Paredes et al., 2023; Dipankar et al., 2026).

101 We use the version of ICON Model developed within the EXCLAIM project (Dipankar et al., 2025), which features a  
102 complete refactoring of the numerical core into GT4Py (icon-exclaim v0.2.0)(Dipankar, 2025). Two global experiments were  
103 conducted on the Swiss National Computing Center’s new HPC infrastructure, ALPS. A ten-year (2006–2016) spin-up sim-  
104 ulation was first performed at a 10 km horizontal grid spacing. A 2.5 km grid spacing simulation following the DYAMOND  
105 protocol (Takasuka et al., 2024b) is conducted for a span of 4 years (January 20, 2020, to April 1, 2024), with its soil state  
106 taken from the 10 km course grid simulation integrated for 10 years (Pothapakula et al., 2026). The 2.5 km simulation uses  
107 240 GH200 GPU nodes (960 GPUs in total), achieving a throughput of 0.25 simulated years per day. This setting was chosen  
108 for computational efficiency, and throughput can be increased by increasing the number of nodes. More information on the  
109 computational aspects of the specific model used for this simulation can be found in Dipankar et al. (2026).

110 The 2.5 km simulation uses lower boundary conditions from daily updated sea surface temperatures and the sea-ice fraction  
111 from the ESA Climate Change Initiative (ESA-CCI) product at a horizontal grid spacing of  $1/20^\circ$  (Merchant et al., 2019).  
112 Furthermore, the setup includes 120 vertical levels extending up to 85 km with a terrain-following hybrid setup and the smooth  
113 level vertical (SLEVE) coordinate (Schär et al., 2002). The single-moment cloud Seifert (2008) bulk microphysics scheme is  
114 used to simulate cloud water, ice, snow, graupel, and rain. The second-order turbulent kinetic energy-based surface transfer and  
115 planetary boundary layer parameterization are used to represent turbulence (Raschendorfer et al., 2003). Land processes are  
116 simulated using the TERRA Multi Layer (TERRA-ML) model (Schrodin and Heise, 2001; Grasselt et al., 2008; Schulz and  
117 Vogel, 2020), which employs eight soil layers and governs the exchange of heat, moisture, and momentum. The TERRA-ML  
118 model employs a tile approach to accurately estimate cell-averaged surface fluxes and account for deviations in sub-grid-  
119 scale surface characteristics. The shallow and deep convection schemes are turned off in the 2.5 km simulation, allowing an  
120 explicit treatment of convection. Additionally, subgrid-scale orographic drag and non-orographic gravity wave drag schemes  
121 are disabled. We used a numerical time step of 20 seconds, updated cloud cover and the microphysics schemes every time step,  
122 and applied the radiation scheme every 6 minutes. The external parameters required by ICON, namely the topographic height  
123 of the Earth’s surface, surface roughness, vegetation cover, and land/sea/lake distribution, were prepared using the External

124 Parameters for Numerical Weather Prediction and Climate Application software tool (Asensio et al., 2020). Finally, we use  
125 the global Max-Planck-Institute Aerosol Climatology version 2 (MAC-v2) dataset with 1 ° grid spacing at a monthly temporal  
126 frequency (Kinne, 2019).

127 The 2.5 km model configuration is close to the ICON-CLM (Climate Limited-area Modelling) community setup and benefits  
128 from the vast experience of the community’s participation in CORDEX (COordinated Regional Climate Downscaling EXper-  
129 iment) activities (Giorgi et al., 2009) across multiple CORDEX regional domains. We did not perform any additional model  
130 tuning for this simulation. We saved output variables following the DYAMOND III protocol (Takasuka et al., 2024b).

## 131 **2.2 Observational Datasets**

132 We use a range of observational datasets alongside reanalysis to assess our simulation’s performance.

### 133 **2.2.1 ERA5**

134 The ERA5 reanalysis is the fifth-generation global atmospheric reanalysis produced by the European Centre for Medium-Range  
135 Weather Forecasts (ECMWF). It provides hourly estimates of a large number of atmospheric, land-surface, and ocean-wave  
136 variables at a horizontal resolution of about 31 km, spanning from 1940 to the present. ERA5 represents a major improvement  
137 over its predecessor, ERA-Interim, particularly in spatial and temporal resolution and in uncertainty estimates (Hersbach et al.,  
138 2020). We use ERA5 data to evaluate 2 m above surface temperature.

### 139 **2.2.2 Brightness Temperature**

140 We use two observational products of brightness temperature (T<sub>b</sub>) in this study. The NCEP/CPC Level-3 merged infrared  
141 T<sub>b</sub> dataset (Janowiak et al., 2017) provides high-resolution data for deep convective cloud identification and tropical wave  
142 tracking. The NOAA outgoing longwave radiation (OLR) dataset has a much lower resolution (Liebmann and Smith, 1996).  
143 It enables the continuous detection of equatorial waves over the simulation period, including slow-evolving variability such as  
144 the Madden-Julian Oscillation.

145 The NCEP/CPC dataset provides gridded equivalent blackbody temperature fields from merged geostationary infrared satel-  
146 lites (Janowiak et al., 2017). It covers latitudes from 60° S to 60° N, with a 4 km horizontal grid and data every 30 minutes. The  
147 product merges observations from multiple geostationary platforms (e.g., METEOSAT, GMS/MTSAT/Himawari, GOES) over  
148 their operational periods. We use full-hour data to track MCSs, non-MCS precipitating cold clouds, and equatorial waves, and  
149 use 30-minute observations to fill gaps in full-hour records.

150 The NOAA OLR dataset provides twice-daily estimates of top-of-atmosphere infrared emission from polar-orbiting satellites  
151 at 2.5° horizontal resolution (Liebmann and Smith, 1996). The dataset spans from 1974 to the present, covers 60° S–60° N, and  
152 provides a consistent long-term record of tropical convective variability. In this study, OLR serves as a large-scale diagnostic  
153 for equatorial wave activity.

### 154 **2.2.3 GPM-IMERGv7 Precipitation**

155 The Integrated Multi-satellite Retrievals for GPM (IMERG) dataset is part of the NASA/JAXA Global Precipitation Mea-  
156 surement mission. It combines observations from a constellation of passive microwave and infrared sensors with gauge data  
157 to provide global precipitation estimates. We use IMERG Final Run version 7, which offers high spatio-temporal resolution  
158 ( $0.1^\circ$ , 30-minute) precipitation fields from the year 2000 to the present (Huffman et al., 2020).

### 159 **2.2.4 HadISD Station Observations**

160 The HadISD (Hadley-Centre Integrated Surface Database) is a global sub-daily station dataset based on the NOAA Integrated  
161 Surface Database (ISD), providing quality-controlled observations of key climatological variables such as temperature, dew  
162 point, sea-level pressure, wind speed and direction, and cloud data at individual stations (Dunn et al., 2016; Dunn, 2024). The  
163 dataset currently spans from 1931 to the present and has undergone extensive automated quality control to detect and remove  
164 erroneous values. However, it is not homogenised, and its station density varies over time. We use hourly precipitation and  
165 10 m above surface wind speed records from HadISD v3.4.1 for model validation. Only stations with more than 50% valid  
166 data coverage during the evaluation period are considered. The location/density of the included station network is shown in the  
167 relevant sections. Station data is compared to data from the nearest ICON grid cell on the native model grid.

### 168 **2.2.5 Surface fluxes: Incoming shortwave and longwave radiation, and latent and sensible heat**

169 We utilize data from 430 flux towers in our model evaluation, sourced from two datasets: FLUXNET (Pastorello et al., 2020)  
170 and AmeriFlux (Chu et al., 2023). These towers provide 30-minute measurements of shortwave and longwave radiation, as well  
171 as surface latent and sensible heat fluxes. Data from these towers is available from 1991 to 2024, with an average record length  
172 of approximately 7 years. The sites are distributed across 43 countries, with denser coverage in North America, Europe, eastern  
173 Asia, and Australia, and sparser representation in Africa and western Asia. It is important to note that inter-annual variability  
174 in surface fluxes contributes to differences between simulations and observations. For reference, across the 430 observational  
175 stations the inter-annual variability, quantified as the standard deviation of annual means, has median values of  $5.2 \text{ W m}^{-2}$  for  
176  $\text{SWin}$ ,  $3.5 \text{ W m}^{-2}$  for  $\text{LWin}$ ,  $6.7 \text{ W m}^{-2}$  for  $\text{LE}$ , and  $5.4 \text{ W m}^{-2}$  for  $\text{H}$ , with interquartile ranges of 3.7–6.8, 2.4–4.6, 4.0–10.5,  
177 and 3.4–8.7  $\text{W m}^{-2}$ , respectively.

178 Additionally, we use gridded surface-downwelling shortwave radiation data from the EWEMBI (Earth2Observe, WFDEI  
179 and ERA-M-B-Ias-corrected) meteorological dataset (Ian, 2016; Lange, 2018) during the period 2012–2016. EWEMBI pro-  
180 vides globally gridded data at  $0.5^\circ$  spatial and daily temporal resolution (calculated as 24-hour averages of hourly fields derived  
181 from 3-hourly fluxes). It combines Earth2Observe data (Schellekens et al., 2017), which uses WFDEI (Weedon et al., 2014)  
182 over land and ERA-Interim over the ocean (Dee et al., 2011), with radiation fields bias-corrected using Surface Radiation  
183 Budget (SRB) observations data released by The GEWEX SRB Project at NASA Langley Research Center (LaRC) (Tren-  
184 berth, 2011) through daily-scale quantile mapping. Although the EWEMBI period (2012–2016) differs from the simulation  
185 period, we include it in the evaluation because interannual variability in surface shortwave radiation is small. The inter-annual

186 standard deviation of the global mean surface-downwelling shortwave radiation is  $0.3 \text{ W m}^{-2}$ , and the distribution of grid-cell  
187 inter-annual variability shows a mean of  $4.3 \text{ W m}^{-2}$  (IQR:  $2.4 \text{ W m}^{-2}$ – $5.0 \text{ W m}^{-2}$ ). Differences exceeding these ranges can  
188 therefore be interpreted as significant rather than reflecting natural year-to-year variability.

## 189 **2.2.6 IBTrACS Tropical Cyclone Characteristics**

190 The IBTrACS (International Best Track Archive for Climate Stewardship) dataset is a comprehensive global compilation of  
191 tropical cyclone “best track” data, aggregated from multiple official agencies across all ocean basins. It provides information on  
192 storm position, intensity (e.g., maximum sustained winds and/or minimum central pressure), and other parameters, typically  
193 at 3-hour or 6-hour intervals, spanning from the mid-19th century to the present (Knapp et al., 2010; Gahtan et al., 2024).  
194 The project also records the original reports from contributing agencies and summary statistics (such as the mean track and  
195 range across agencies) to facilitate intercomparison. We use U.S. records from IBTrACS v4.01 (specifically the variables  
196 ‘usa\_wind’ and ‘usa\_pres’) because they are the most up-to-date and include information on recent global tropical cyclone  
197 activity. Recorded speed correspond to maximum sustained wind averaged over 1 minute at 10 m above surface.

## 198 **2.3 Methods**

### 199 **2.3.1 Atmospheric feature tracking with the MOAAP algorithm**

200 The Multi-Object Analysis of Atmospheric Phenomenon (MOAAP; Prein et al. (2023b)) algorithm is an automated, object-  
201 based framework that identifies and tracks a wide range of atmospheric systems using a minimal set of commonly available  
202 reanalysis and model variables. MOAAP combines 12 key atmospheric variables from observations (here, ERA5 reanalysis,  
203 GPM IMERG precipitation, and GPM\_MERGIR cloud-top Tb) and the ICON model to consistently detect and track features  
204 such as tropical and extratropical cyclones, cut-off lows, anticyclones, frontal zones, jet streams, moisture streams, mesoscale  
205 convective systems (MCSs), and equatorial waves.

206 Feature detection is based on a connected-component approach applied in space and time. The algorithm first thresholds  
207 relevant variables to form binary masks of regions that exceed physically motivated intensity thresholds. It then labels contigu-  
208 ous three-dimensional (latitude–longitude–time) structures using the `ndimage.label` function from SciPy (Virtanen et al.,  
209 2020). In a second step, features are segmented based on the presence of multiple minima/maxima within an object using  
210 the `skimage.segmentation` and `skimage.feature` functionalities, with watershed segmentation applied. Phenom-  
211 ena are then identified according to temporal persistence rules and phenomenon-specific geometric, temporal, and intensity  
212 thresholds. Each identified object is assigned physical characteristics such as area, duration, maximum intensity, and center of  
213 mass, which enable subsequent statistical and climatological analyses. MOAAP provides a unified, reproducible framework  
214 for quantifying and intercomparing the contributions of different atmospheric phenomena to mean and extreme precipitation  
215 across spatial and temporal scales.

216 The MCS analysis in section 3.7 is performed on a global  $0.1^\circ$  regular grid that corresponds to the GPM-IMERG grid.  
217 GPM-MERGIR and ICON data are conservatively regridded to this grid. MCSs are defined as in Prein et al. (2024) following

218 four criteria: 1) Continuous Tb  $\leq$  241 K area  $\geq$  40,000 km<sup>2</sup> for  $\geq$  4 hours; 2) maximum hourly precipitation beneath the Tb  $\leq$   
219 241 K area  $>$  10 mm h<sup>-1</sup> for  $\geq$  4 hours; 3) hourly precipitation volume  $>$  20,000 km<sup>2</sup> mm h<sup>-1</sup> at least once during the MCS  
220 lifetime; 4) minimum Tb  $<$  225 K at least once during the MCS lifetime.

221 Additionally, the hourly heavy precipitation analysis in section 3.9 is performed on a standard 0.25 ° mesh that corresponds  
222 to the ERA5 grid. The only phenomenon not included in MOAAP that we were unable to identify is atmospheric rivers, as  
223 ICON lacks an IVT diagnostic. More details about MOAAP can be found in (Prein et al., 2023b, 2024; Feng et al., 2025).

### 224 2.3.2 Deriving central pressure, maximum wind, and pressure–wind pairs

225 We use tropical cyclones (TCs) identified by MOAAP to calculate TC intensity centered on the TC sea level pressure (SLP)  
226 minima at each time step (hour). Distances and azimuths are computed using great-circle geometry, and land-sea ocean points  
227 are defined via a land-sea mask with a 30 km coastal buffer. The maximum sustained wind  $V_{\max}$  is the peak 10-m wind speed  
228 from hourly instantaneous model output within the inner-core disk given by the Reference Disk Radius (RDR), defined as

$$229 \text{RDR} = \min(\text{RMW}, r_{\partial p}),$$

230 where  $\text{RMW} = \arg \max_r |\overline{u_t}|(r)$  is the radius of maximum mean tangential wind and  $r_{\partial p} = \arg \max_r |\partial \overline{p} / \partial r|$  is the radius of  
231 strongest radial SLP gradient (Knaff and Zehr, 2007; Schenkel and Hart, 2012).

## 232 3 Results

233 We start this section with a climatological analysis of near-surface temperature, surface fluxes, and precipitation, followed  
234 by assessing higher-order statistics of hourly precipitation and surface wind speed, and ending with evaluating the fidelity of  
235 simulating atmospheric storms such as TCs, MCSs, and extreme precipitation-producing systems.

### 236 3.1 2 m above surface temperature (T2M)

237 The global average pattern of T2M is well simulated with a Spearman pattern correlation coefficient of 0.998 and a root mean  
238 squared error of 1.48 °C for land grid points (Fig. 1). As expected, ocean regions exhibit particularly small differences due to  
239 the pre-described sea surface temperature. Striking are cold differences in ICON during polar winters that might be related to  
240 the representation of sea ice and snow in addition to differences stemming from uncertainties in ERA5 T2M in these regions  
241 (Fig. 1d,f). Larger differences also occur during boreal winters over land areas with up to 3 °C negative differences in eastern  
242 Canada and large positive differences in Siberia and Alaska.

243 During boreal summers, temperatures exceeding 3 °C warm differences emerge in continental regions such as the central  
244 U.S. and Eurasia (Fig. 1f). Part of these differences is likely related to a misrepresentation of land-atmosphere interactions, such  
245 as the lack of lateral groundwater flow and the corresponding reduced evapotranspiration in land-atmosphere coupling hot-spots  
246 such as the central U.S., which can cool down these regions by several degrees Celsius during the summer season (Barlage  
247 et al., 2021; Schlemmer et al., 2018). Additionally, misrepresented cloud radiative forcings frequently (Fig. S1) contribute

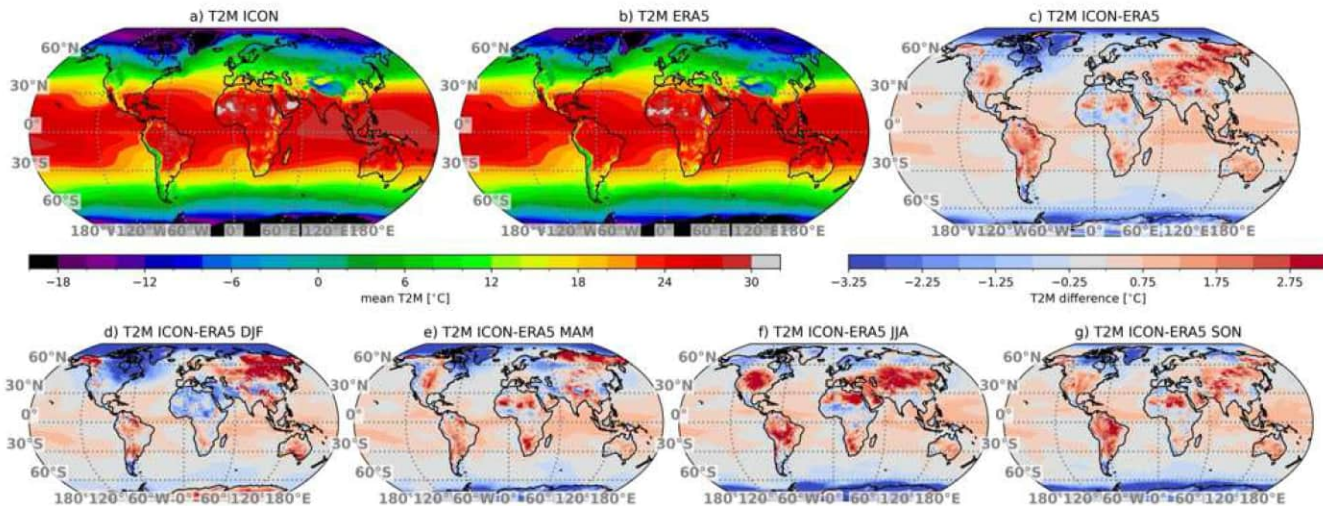


**Figure 1.** Annual mean daily T2M in ICON (a), ERA5 (b), and their difference (c) during the simulation period. Seasonal average T2M differences are shown in (d–g).

248 to surface temperature biases in models with convection parameterizations (e.g., Ahlgrim and Forbes, 2012) and km-scale  
 249 models (e.g., Sakradzija et al., 2020; Lucas-Picher et al., 2024).

250 It is important to note that the differences shown here and in the following sections are partly related to the short simulation  
 251 period of four years. Climate internal variability can cause large differences at local scales (Deser et al., 2012) even though  
 252 observed sea surface temperatures are used.

### 253 3.2 Surface fluxes: Incoming shortwave and longwave radiation, and latent and sensible heat

254 Fig. 2 shows the daily mean surface incoming shortwave radiation (SWin) for (a) ICON, (b) the EWEMBI observational  
 255 dataset, and (c) their difference. Overall, SWin is underestimated over oceans, especially along the Intertropical Convergence  
 256 Zone, and overestimated over land, particularly in mountainous regions. This overestimation over land is also evident when  
 257 comparing the simulation to flux tower observations (Fig. 2d,e). The median difference in land mean SWin is approximately  
 258  $6.8 \text{ W m}^{-2}$ , with a median difference of around  $28.2 \text{ W m}^{-2}$ . The overall median difference is consistent with the mean bias  
 259 error of approximately  $7.8 \text{ W m}^{-2}$  reported for CMIP6 models by He et al. (2023). Previous studies have shown that shallow  
 260 clouds are frequently a main contributor to continental surface energy biases in km-scale models (e.g., Sakradzija et al., 2020;  
 261 Lucas-Picher et al., 2024).

262 Fig. 2d and e show the spatial distribution of station median total and noon differences in longwave downward radiation  
 263 (LWin), latent heat flux (LE), and sensible heat flux (H). LWin is slightly underestimated. LE shows a median difference close  
 264 to zero across stations, with regionally over- and underestimations of more than  $10 \text{ W m}^{-2}$  that cancel each other on average.  
 265 This spatial compensation suggests region-dependent limitations in the representation of land-surface controls on evaporation,

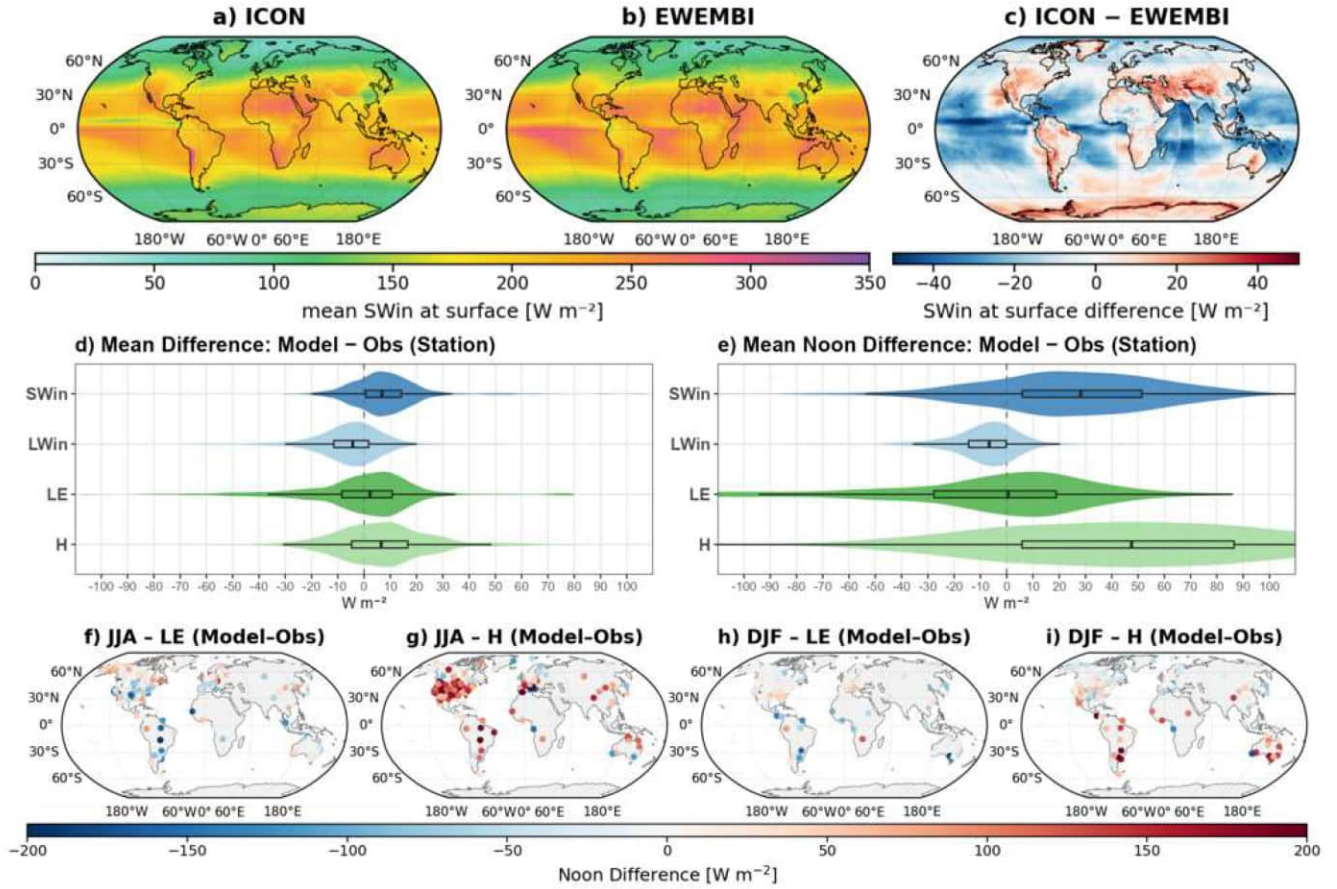


**Figure 2.** (a–c) Daily mean incoming shortwave radiation at the surface (SWin) from (a) ICON (2020–2024), (b) the EWEMBI (2012–2016) observational dataset, and (c) their difference (ICON - EWEMBI). (d–e) Violin plots of station-based differences (model - observations) for mean (d) and mean local solar time noon (e) surface fluxes: SWin, incoming longwave radiation (LWin), latent heat flux (LE), and sensible heat flux (H). Boxes indicate the interquartile range and median difference. (f–i) Station-based mean noon differences (model - observations) for LE and H during JJA (June, July, August) and DJF (December, January, February).

266 rather than a uniform model bias. In contrast, H is more consistently overestimated, particularly during noon, agreeing with the  
 267 overestimation in SWin.

268 The spatial pattern of station-based mean noon differences in LE and H during JJA shows a pronounced underestimation of  
 269 LE and an overestimation of H at most stations in ICON (Fig. 2f,h) in agreement with the T2M differences shown in Fig. 1.  
 270 We suspect that parts of the systematic dry-summer biases are due to the absence of a lateral subsurface water-flux scheme in  
 271 TERRA. Previous studies have shown that the lack of such lateral groundwater redistribution can lead to substantial surface  
 272 flux and temperature biases at km-scale grid spacing (Barlage et al., 2021; Soares et al., 2024). In contrast, there is more

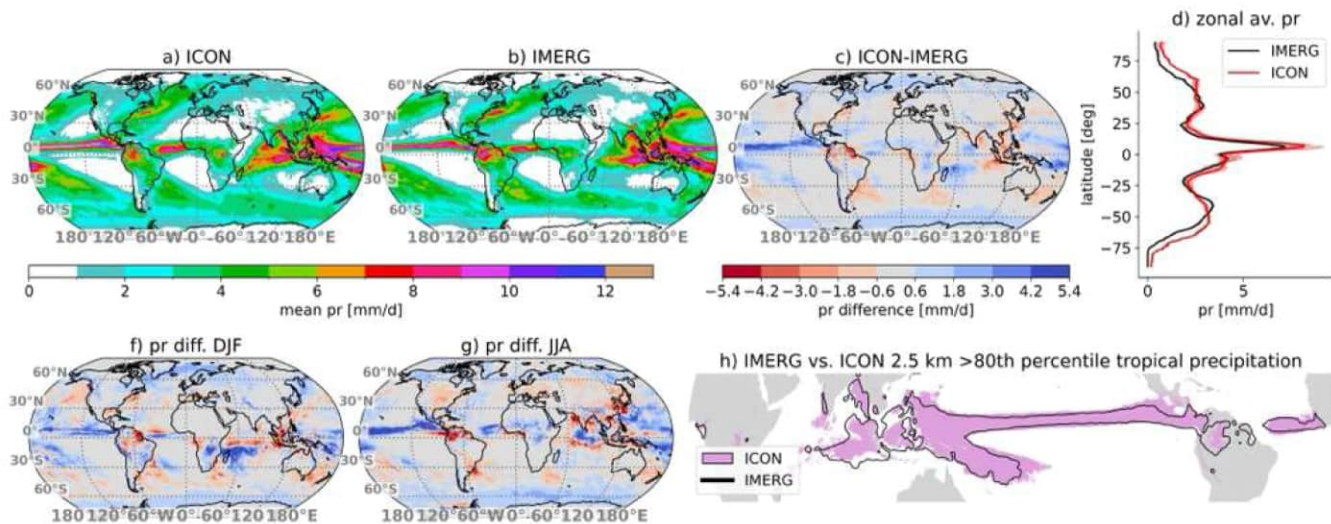


**Figure 3.** Annual mean daily precipitation in ICON (a), IMERG (b), and their difference (c) during the simulation period. DJF and JJA average precipitation differences are shown in (f) and (g), respectively. Mean zonal average precipitation is shown in (d) with inter-annual spread shown in contours. The area that covers the 80th percentile of tropical average precipitation ( $\pm 20^\circ$ ) from ICON (purple) and IMERG (black contour) is shown in (h).

273 station-to-station variability for winter biases. The spatial patterns and characteristics of surface flux differences are consistent  
 274 with biases in temperature and precipitation.

### 275 3.3 Precipitation (PR)

276 Annual and seasonal differences between ICON and GPM-IMERG are shown in Fig. 3. The Pearson pattern correlation of  
 277 annual average precipitation is 0.91 (0.87 over land cells) and the corresponding relative RMSE is 41 %. Most noticeable are  
 278 wet differences over most tropical ocean regions except for the west Maritime Continent (Fig. 3c). This is consistent with the  
 279 negative SWin differences shown in Fig. 2c. Land precipitation is relatively well simulated overall, although dry differences  
 280 emerge in several continental regions during boreal summer (Fig. 3g). In some of these regions, including parts of the central  
 281 U.S. and Eurasia, the dry differences coincide with warm T2M differences (Fig. 1f), higher SWin, lower LE, and higher H,  
 282 suggesting a contribution from land-atmosphere coupling and cloud radiation biases.

283 Zonal average precipitation agrees very well between GPM-IMERG and ICON, partly because of error cancellation effects  
 284 (Fig. 3d). The differences are typically smaller than the inter-annual variability (shading in Fig. 3d) except for high-latitudes  
 285 where IMERG is known to underestimate precipitation accumulations due to issues in remote sensing solid precipitation (Song  
 286 et al., 2021) complicating a reliable evaluation. The location of the wet regions in the tropics (defined as the 80th percentile of  
 287 tropical average precipitation; Fig. 3h) is remarkably well captured with a single tropical rainband.

288 This is a big achievement since simulating a realistic rainband is challenging, even at a km grid spacing, as Segura et al.  
289 (2022, 2025a, b) found a double ITCZ in the Indo-Pacific using km-scale ICON simulations with model physics different  
290 from ours. They found a lack a surface fluxes (caused by too little surface winds) in this region, which they resolved by  
291 increasing the minimum surface wind speed in the lowest model level from  $1 \text{ m s}^{-1}$  to  $4 \text{ m s}^{-1}$  (Segura et al., 2025a). Our  
292 model settings, which are similar to ICON’s NWP setup, do not feature this issue. While it is unclear exactly what causes  
293 the differences in model performance among the ICON setups, a key difference lies in the turbulence parameterizations and  
294 surface-layer schemes, while Takasuka et al. (2024b) found large sensitivities to the formulation of microphysics. The location  
295 of mid-latitude precipitation bands associated with the storm tracks is reasonably well simulated (Fig. 3a,b).

296 Comparing peak hourly precipitation over the four-year evaluation period between GPM-IMERG and ICON shows that our  
297 simulation yields substantially larger values, particularly in the tropics and subtropics (Fig. 4a,b). This is predominantly caused  
298 by too low heavy hourly precipitation in GPM-IMERG since comparisons with hourly precipitation gauge observations from  
299 the HadISD dataset show that ICON reliably reproduces observed intense precipitation rates across various climate regions.  
300 At the same time, GPM-IMERG fails to capture intense rates, particularly at lower latitudes (Fig. 4c–f), which is in agreement  
301 with previous research (Guiloteau and Foufoula-Georgiou, 2020; Dominguez et al., 2024; Yu et al., 2025). However, a proper  
302 evaluation of hourly precipitation using station data is not possible in many parts of the globe due to insufficient data coverage  
303 and a lack of data sharing (e.g., Prein and Gobiet, 2017). Our presented analysis is primarily based on data from the U.S. and  
304 Europe (see Fig. S2). Results for additional climate regions, often based on only a few stations, are shown in Fig. S3.

305 Using the same station network, we assess the June-July-August (JJA) season-average precipitation diurnal cycle (Fig. 5; we  
306 use  $0.1 \text{ mm h}^{-1}$  as the threshold for precipitation intensity and frequency statistics). The performance of ICON is regionally  
307 dependent and shows good agreement for capturing precipitation amount, frequency, and intensity in the North Central Amer-  
308 ica (NCA) region that is heavily influenced by the North American Monsoon (Fig. 5g–i). In Eastern North America (ENA),  
309 precipitation frequency is well captured compared to station data. Still, precipitation intensity is overestimated, resulting in an  
310 overly amplified evening and nocturnal peak in precipitation amplitudes (Fig. 5a–c). Western Central Europe (WCE) shows a  
311 too-early peak in precipitation that decays too quickly. The precipitation amount is also low-biased due to the too low precipi-  
312 tation frequency. Generally, ICON shows greater fidelity in capturing the diurnal cycle of convective precipitation in southern  
313 regions (ENA and NCA) than GPM-IMERG.

314 From Fig. 5, we see that the peak timing of convective precipitation amount is relatively well captured by GPM-IMERG,  
315 consistent with previous findings (e.g., Dominguez et al., 2024) although IMERG has been reported to have a phase lag relative  
316 to Ku-band radar in many regions which should be kept in mind (Hayden and Liu, 2021). This allows us to evaluate ICON  
317 on a near-global scale (Fig. 6). We perform this analysis during seasons dominated by convective precipitation, namely JJA at  
318  $>30^\circ\text{N}$ , December-January-February (DJF) at  $<30^\circ\text{S}$ , and annually in the tropics. GPM-IMERG and ICON feature afternoon  
319 precipitation peaks over land. In contrast, tropical ocean regions feature predominantly nighttime and early-morning peaks.  
320 Some land regions also feature nocturnal precipitation peaks, particularly in the lee of mountain ranges (e.g., the central U.S.,  
321 the La Plata basin, eastern China, and the Sahel and Western Africa), which are related to nocturnal mesoscale convective  
322 system activity. ICON can capture these nocturnal peaks reasonably well, but the spatial extent of nocturnal regions is often

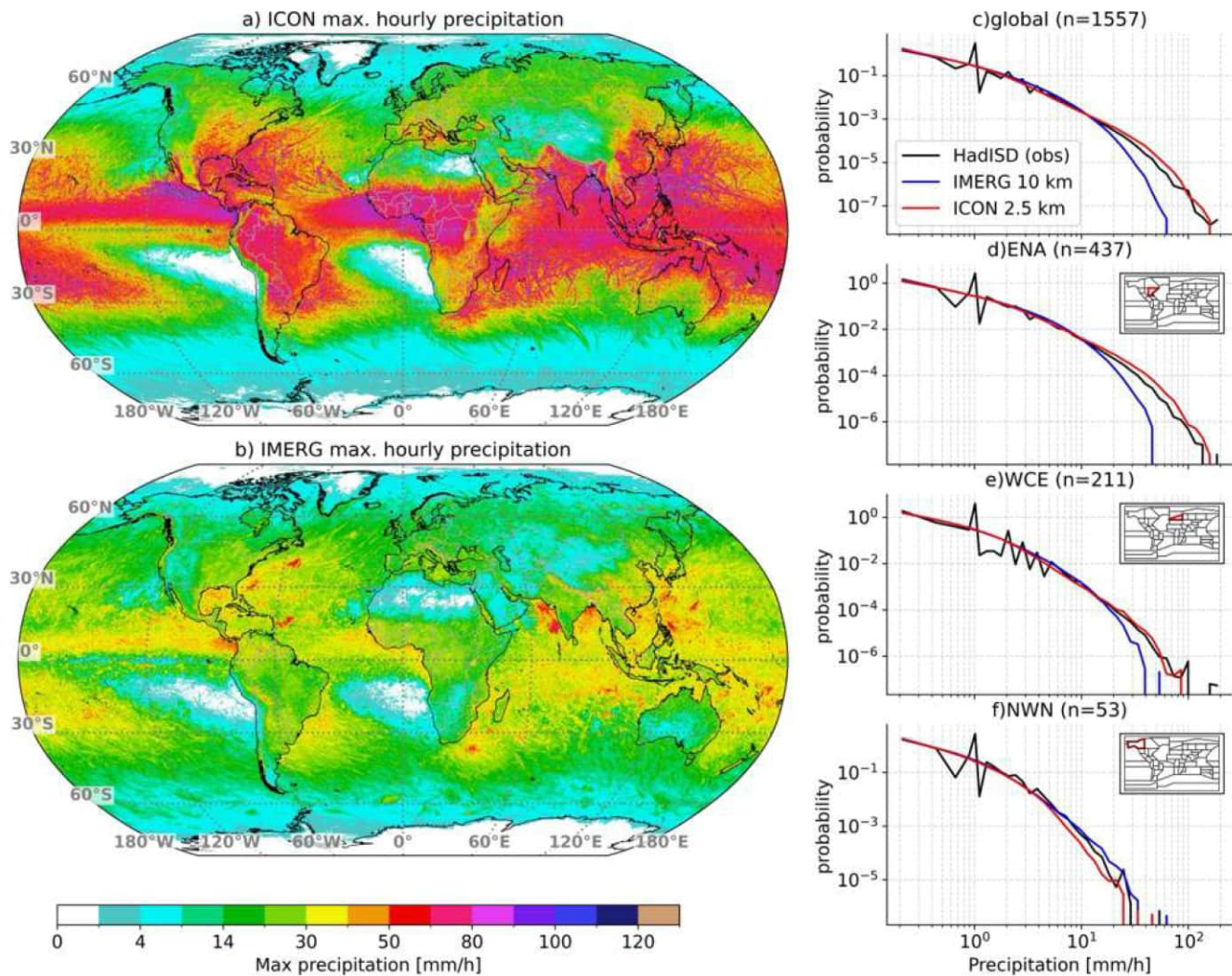


**Figure 4.** Hourly maximum precipitation accumulation during the simulation period from ICON (a) and IMERG (b) on the  $0.1^\circ$  IMERG grid. Probability density functions for hourly precipitation comparing ICON (red) and IMERG (blue) against HadISD station observations (black) globally (c) and in the Eastern North America (ENA, d), Western Central Europe (WCE, e), and North Western North America (NWN, f) region. The locations of these regions are shown in the inlet maps in (b–f). The underlying station density in the HadISD dataset is shown in Fig. S2.

323 too small, particularly in the Amazon Basin and the central U.S. The relative amplitude of the convective precipitation diurnal  
 324 cycle (diurnal amplitude divided by mean precipitation) is also relatively similar, with a tendency for larger values in ICON  
 325 compared to GPM-IMERG.

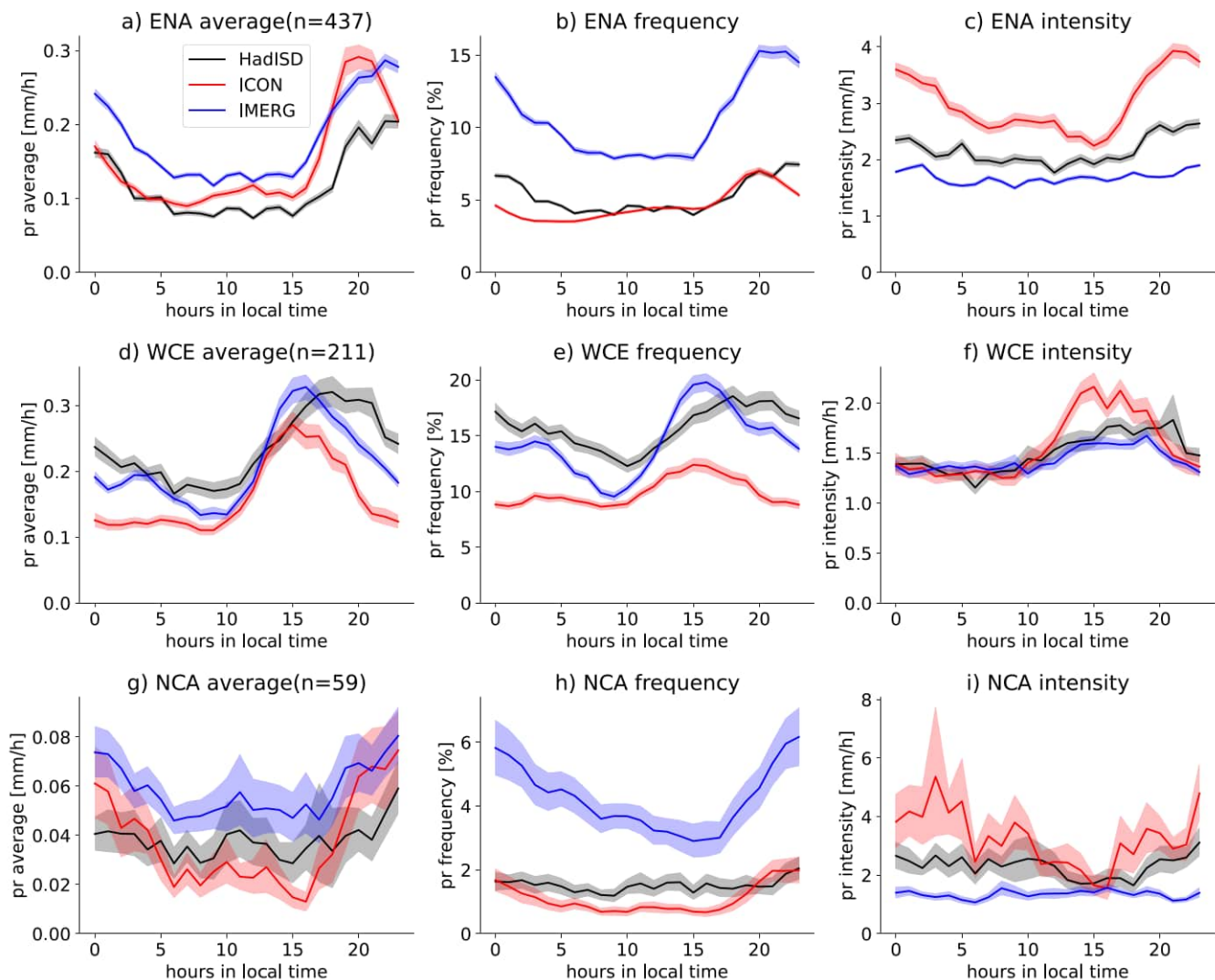


**Figure 5.** Hourly precipitation diurnal cycle during June, July, and August of average precipitation (a, d, g), precipitation frequency (b,e,h), and precipitation intensity (c,f,i). Results are shown for the Eastern North America (a–c), Western Central Europe (WCE), and North Central America (NCA) region. Precipitation frequency and intensity statistics are based on a precipitation threshold of  $\geq 0.1 \text{ mm h}^{-1}$ . Data are based on HadISD records (black lines) with more than 50% coverage. Missing values in HadISD are also removed in the ICON (red lines) and IMERG (blue lines) data. Contours show station sampling uncertainties based on the 10th to 90th percentile values from 10,000 bootstrap samples (with replacement).

326 In summary, we recommend using GPM-IMERGv7 hourly precipitation with caution in model evaluation studies, given its  
 327 tendency to overestimate precipitation frequency and underestimate precipitation intensity. Where possible, in-situ hourly rain  
 328 gauge observations should be used.

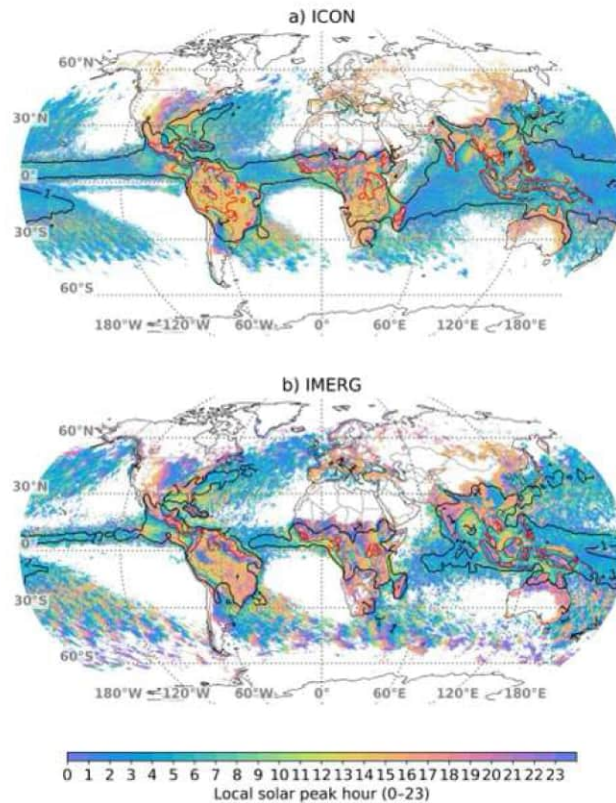


**Figure 6.** Color-coded local peak time of precipitation diurnal cycle in ICON (a) and IMERG (b). Colored regions show areas where the precipitation diurnal cycle amplitude is larger than 40 % of the mean precipitation. Black/red contours show regions where the amplitude is larger than 100 %/200 % of the mean precipitation. Data from all months is used in the tropics ( $\leq \pm 30^\circ$ ), data from June, July, and August is used for latitudes  $> 30^\circ$ , and data from December, January, and February is used for latitudes  $< -30^\circ$ .

### 329 3.4 Near surface winds (UV10)

330 Tropical cyclones cause the most intense UV10 extremes during the evaluation period (Fig. 7a). Storm tracks of extratropical  
 331 cyclones are also clearly visible in both hemispheres. Over land, mountain regions and plateaus such as the Tibetan Plateau and  
 332 the Andes stand out, as do mid-latitude plains that feature straight-line windstorms (e.g., the central U.S., the La Plata Basin,  
 333 and the Sahel). Also, the coastal regions of Greenland and Antarctica feature peak wind speeds exceeding  $40 \text{ m s}^{-1}$ .

334 Evaluations against UV10 HadISD station observations show overall good agreement with a tendency of heavy wind speeds  
 335 ( $> 20 \text{ m s}^{-1}$ ) to be underestimated in ICON (Fig. 7b). However, regional differences are observed, with lower differences at  
 336 high wind speeds, mostly in Mid-Latitude regions such as CNA and WCE (Fig. 7c,d). The region with the most pronounced  
 337 underestimation of UV10 extremes is Eastern North America (Fig. S5), which might be partly related to a low difference in  
 338 tropical cyclone frequency as we will see in section 3.5, but regional differences in the simulation of extra-tropical cyclones

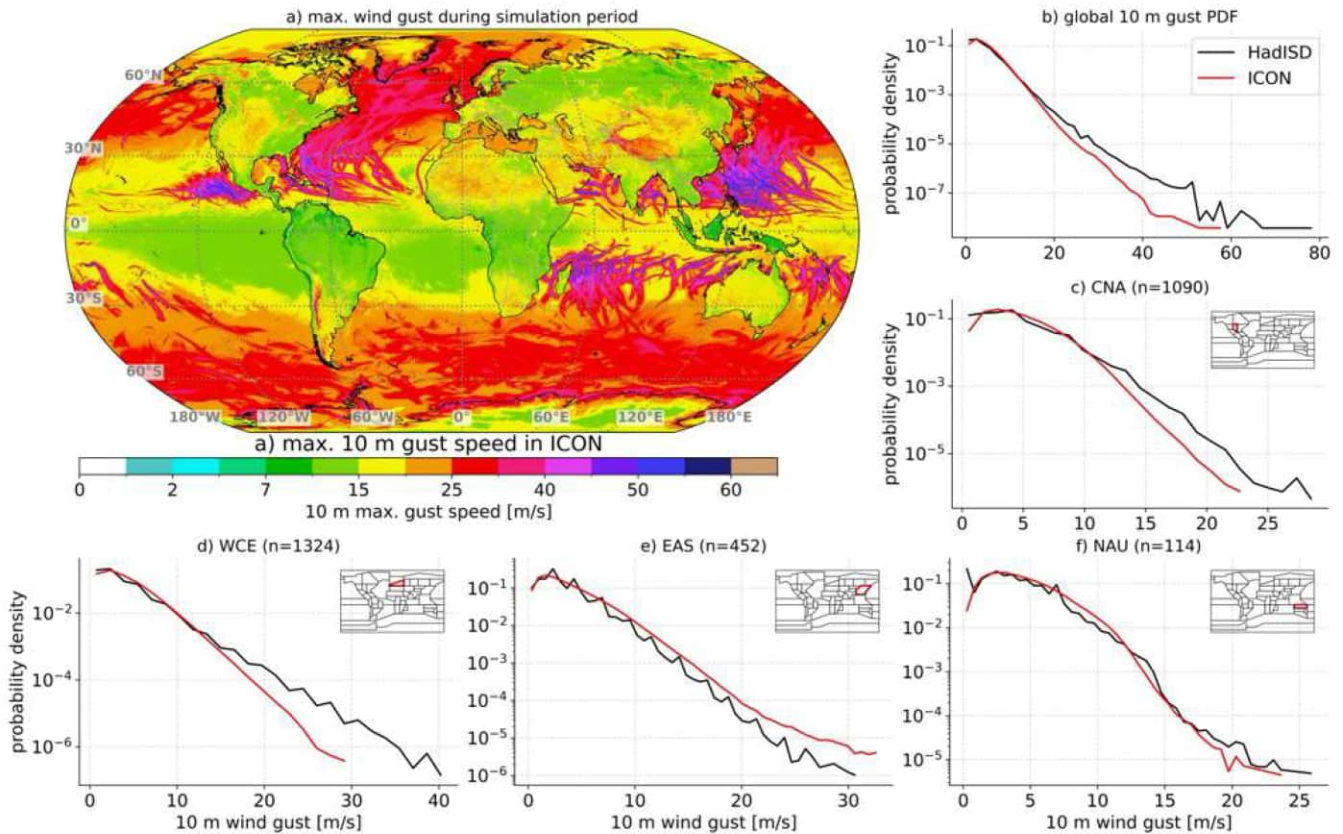


**Figure 7.** Maximum instantaneous simulated 10 m above surface wind from hourly model output during the simulation period (a). Probability density functions for hourly sampled winds from HadISD (black line) and ICON (red line). Statistics are shown for all stations globally (b; see Fig. S4 for station locations) and for the Central North America (CNA; c), Western Central Europe (WCE; d), East Asia (EAS; e), and North Australia (NAU; f) region. The number of stations (n) in each region is shown in the panel titles.

339 could also contribute. Intense winds are well simulated in most tropical and high latitude areas such as East Asia (EAS) and  
 340 Northern Australia (NAU) (Fig. 7e,f). The station density that is available for comparison in HadISD is shown in Fig. S4, and  
 341 statistics for additional IPCC regions are shown in Fig. S6. Also, ICON reproduces the temporal autocorrelation of hourly winds  
 342 well (Fig. S5), indicating that it captures the persistence and day-to-day temporal variability of near-surface wind fluctuations,  
 343 including both the rapid decorrelation at short lags and the diurnal recurrence seen in the observations.

344 The wind speed evaluation should be interpreted with caution, as we compare station data with 2.5 km grid-cell averages.  
 345 Additionally, short-term average wind speeds (e.g., 2-minute averages at U.S. stations, 10-minute averages at many WMO  
 346 stations) are compared with hourly instantaneous model winds. Instantaneous model snapshots tend to produce broader, higher-  
 347 tailed wind-speed PDFs than temporally averaged station observations, while spatial averaging over 2.5 km grid cells damps  
 348 small-scale wind maxima. The combined effect partially compensates for differences. Km-scale modes are generally more

349 comparable to station observations because the scale differences between the simulated processes on the grid and point-based  
350 observations are smaller than in coarser-resolution models.

### 351 **3.5 Tropical cyclones**

352 Tropical cyclone tracks compare well in frequency and location between ICON and IBTrACS, except for the North Atlantic  
353 Basin, which features a low bias (Fig. 8a,b). Note that the longer tracks in IBTrACS are caused by identifying TCs already as  
354 tropical depressions and following them after the extra-tropical transition. In contrast, MOAAP only identifies the main TC  
355 phase. The inter-annual variability of basin total tropical cyclone frequencies is also well captured in ICON, except for the  
356 Southwest Pacific and South Indian Ocean, where the variability is smaller (Fig. 8b).

357 The TC pressure wind relationship is relatively well captured, but ICON wind speeds are too low (Fig. 8c), consistent with  
358 the UV10 analysis in the previous section and simulations with the NICAM model at km-scale (Takasuka et al., 2024a). The  
359 low difference is also reflected in the probability histogram of tropical cyclone lifetime peak wind speeds, which drops off  
360 too rapidly at high wind speeds (Fig. 8d). The IBTrACS distribution shows a bi-modal distribution with a minimum around  
361  $40 \text{ m s}^{-1}$  and a primary peak at low wind speeds. The reason for this primary peak is that the tropical depression and tropical  
362 storm phases of TC are included in IBTrACS. In contrast, the MOAAP tracker is calibrated to identify only storms of tropical  
363 storm intensity. Similar to the comparison to station-based wind observations in the previous chapter, comparing modeled  
364 instantaneous wind fields to IBTrACS observations is challenging. The simulation provides gridded 10 m near-surface winds,  
365 while IBTrACS reports storm-level maximum sustained winds from observational best-track analyses. They are therefore not  
366 directly equivalent, since the model resolves spatial wind structure and average wind speeds within grid cells, whereas IBTrACS  
367 summarizes cyclone intensity. This could explain parts of the low difference in wind speed seen in ICON.

### 368 **3.6 Equatorial waves and the Madden-Julian oscillation**

369 Fig. 9 shows Hoffmüller diagrams of tropical average  $T_b$  in ICON and GPM-MERGIR, with labels indicating equatorial waves  
370 from MOAAP output for May 2020. While Rossby waves are well simulated in ICON, other waves that are strongly coupled  
371 to deep convection are underestimated in both frequency and amplitude. Kelvin and inertia-gravity waves (IGWs) are very  
372 infrequent, and Mixed Rossby-Gravity Waves (MRGs) are only regularly observed over Africa.

373 Global kilometer-scale (storm-resolving) models substantially improve the simulation of convectively coupled equatorial  
374 waves by explicitly representing deep convection, leading to more realistic precipitation spectra, wave propagation, and dy-  
375 namical structures compared to models with parameterized convection (Satoh et al., 2019; Hohenegger et al., 2020; Jung  
376 and Knippertz, 2023). However, despite these advances, biases remain in wave–convection coupling strength, phase speed,  
377 and intermittency, indicating that the representation of equatorial waves at km-scale resolution is improved but still model-  
378 and configuration-dependent rather than fully resolved (Hohenegger et al., 2020; Takasuka et al., 2024a; Jung and Knippertz,  
379 2023).

380 Wheeler–Kiladis space–time spectra computed from the four-year evaluation period confirm these results (Fig. 10). We fol-  
381 low the approach of Takayabu (1994) and Takayabu (1994); Wheeler and Kiladis (1999) and apply it to outgoing longwave

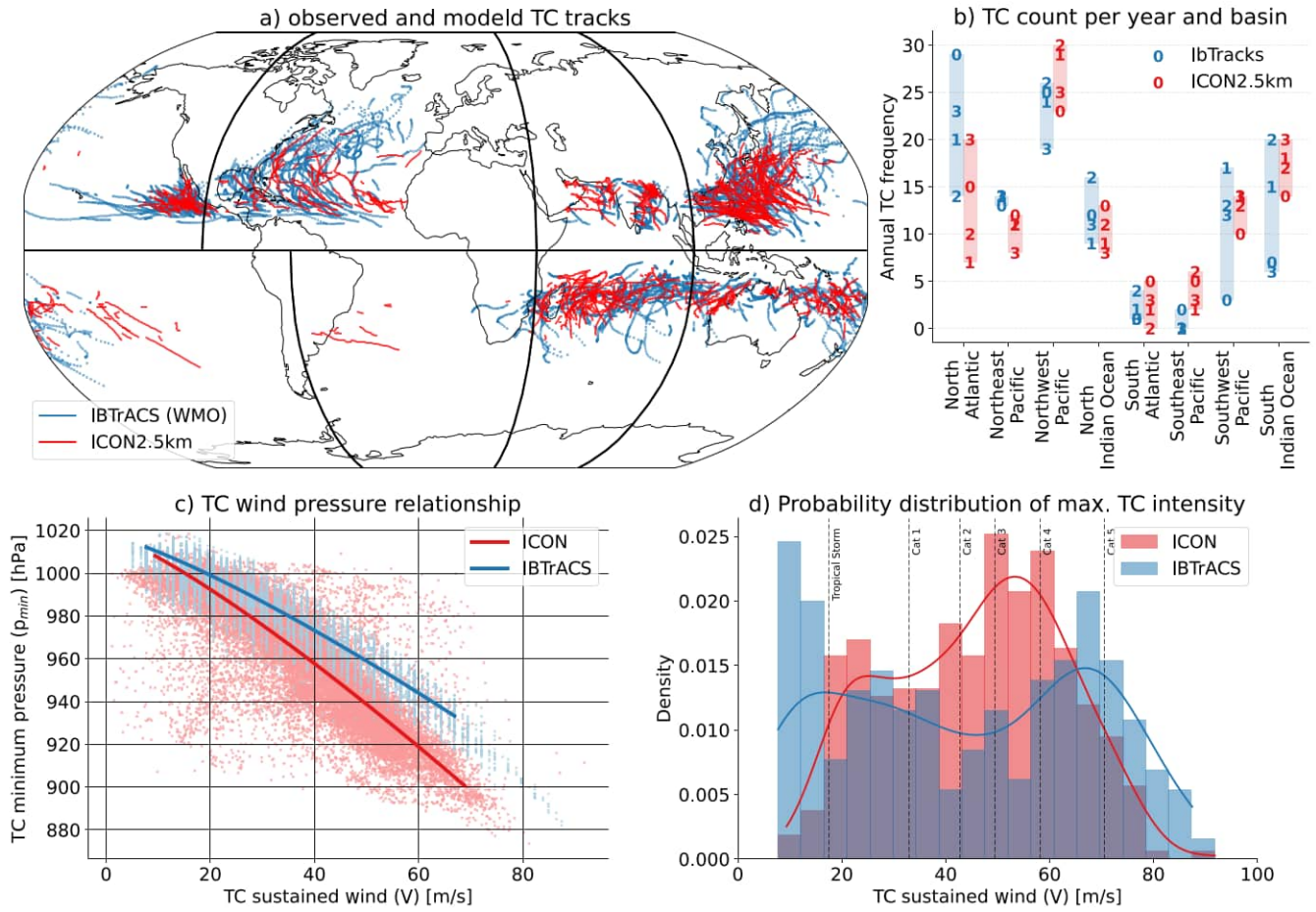


**Figure 8.** Tropical cyclone (TC) tracks from IBTrACS (blue) and ICON (red) during the simulation period (a). Basin annual frequency of tropical cyclones (b) in 2020 (0; only April to December), 2021 (1), 2022 (2), and 2023 (3). Tropical cyclone pressure wind relationship (c) from IBTrACS (blue) and ICON (red). Thick lines show the fitted figure of  $V(p_{min}) = a(p_{ref} - p_{min})^b$  with  $p_{min}$  being the minimum cyclone pressure,  $V$  being the sustained wind speed, and  $p_{ref}$  being the reference pressure at zero wind speed. Probability density of lifetime peak tropical cyclone sustained wind speed in IBTrACS and ICON (d).

382 radiation (OLR) from the ICON simulation and the NOAA-interpolated OLR dataset. Overall, ICON reproduces the observed  
 383 spectral characteristics of equatorial waves reasonably well. Rossby wave activity shows the closest agreement with observa-  
 384 tions, while other modes—such as Kelvin waves, the Madden–Julian Oscillation (MJO), and IGW—are captured but exhibit  
 385 lower amplitudes than in the NOAA OLR data.

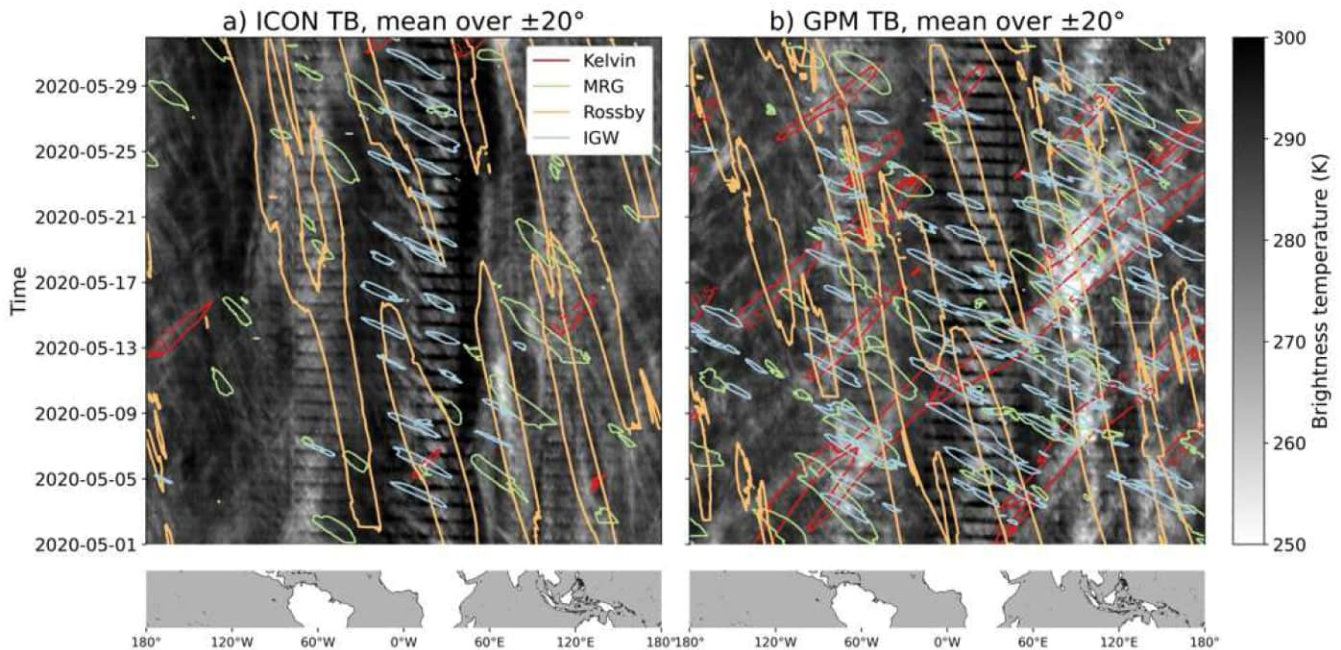


**Figure 9.** Hoffmüller diagrams of tropical average ( $\pm 20^\circ$ ) brightness temperature from ICON (a) and GPM-MERGIR (b) shown in gray contours for May 2020. Contours lines show Kelvin (red), Mixed Rossby Gravity (MRG, green), Rossby (orange), and Inertia Gravity (IGW, blue) waves.

386 **3.7 Mesoscale convective systems (MCSs)**

387 Equatorial waves often organize convection into clusters of MCSs. The latent heating from these MCSs can, in turn, amplify  
 388 and sustain the wave, creating a feedback loop between the large-scale disturbance and convection (Kiladis et al., 2009). The  
 389 general pattern of MCS initiation frequency is well captured in ICON, but initiation is underestimated over tropical oceans and  
 390 overestimated over tropical land regions (Fig. 11a–c). The relative underestimation of oceanic MCS frequency is largest in the  
 391 northern hemisphere, followed by the Southern Hemisphere, and tropics (Fig. 11g–i). In the tropics, oceanic MCS frequencies  
 392 are well simulated between December and March but have a systematic low bias in the other months of the year (Fig. 11h).

393 Simulated land-based MCSs frequencies are most similar to observations in the northern hemisphere. Frequencies are over-  
 394 estimated in the Southern Hemisphere during summer and in the tropics year-round, except in June and July.

395 These frequency biases result in a systematic underestimation of the MCS to total precipitation ratio over almost all ocean  
 396 regions, while this ratio is overestimated over Africa (Fig. 11d–f). The reasons for the MCS frequency biases are unclear, but  
 397 they might be related to biases in tropical waves and the thermodynamic-convection coupling (?), which will be the topic of  
 398 future research.

399 In addition to frequency statistics, we also performed lifetime analysis of oceanic and land-based MCSs in the tropics,  
 400 northern, and Southern Hemispheres (Fig. 12 and Fig. S7 and S8 respectively). We discuss only the results from the tropics

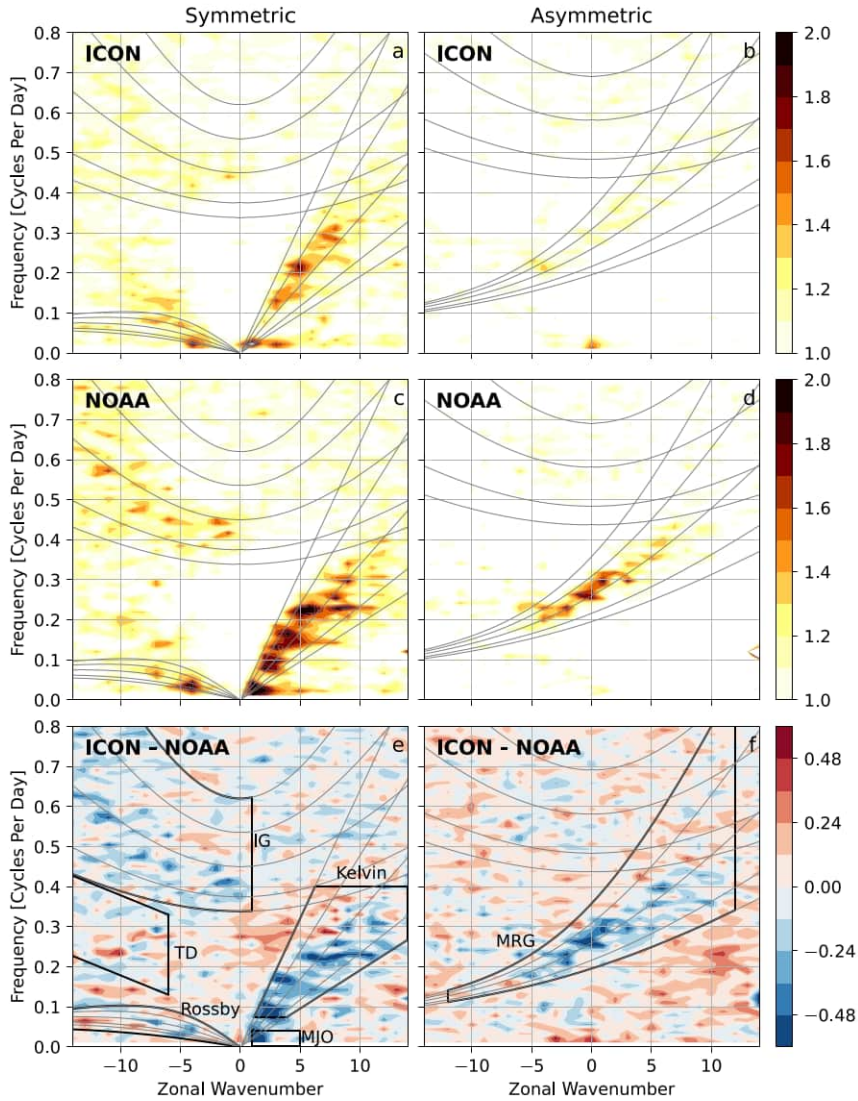


**Figure 10.** Wavenumber–frequency spectra of outgoing longwave radiation (OLR), divided by the background spectrum, from the ICON simulation (a, b) and NOAA satellite observations (c, d), along with their differences (e, f). Spectra are separated into symmetric (a, c, e) and antisymmetric (b, d, f) components. Gray curves indicate theoretical dispersion relations, while bold black outlines denote spectral windows associated with different equatorial wave modes: IG (inertia–gravity waves), TD (tropical depressions), Rossby, MJO (Madden–Julian Oscillation), Kelvin, and MRG (mixed Rossby–gravity waves).

401 here, since they are similar in both hemispheres. Observed MCS sizes are similar over tropical oceans and land (Fig. 12a).  
 402 Simulated MCSs are generally smaller than observed systems. The simulated MCS movement speed is systematically higher  
 403 for most quintiles (Fig. 12b), while the mean precipitation under the MCS cloud shields is lower (Fig. 12c), particularly for

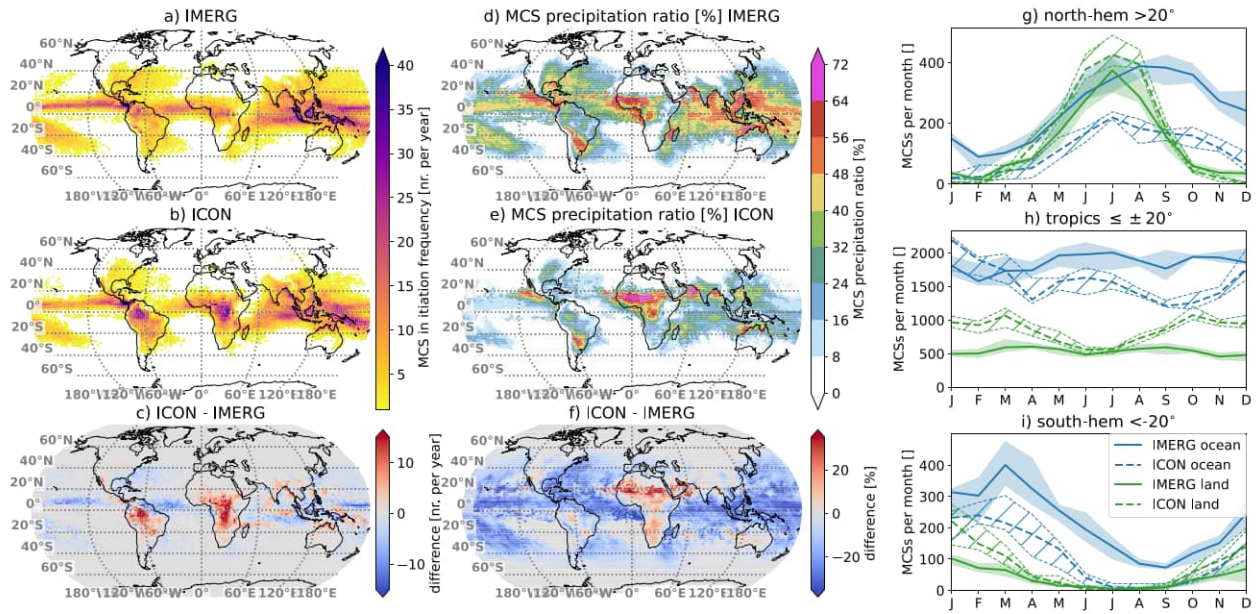


**Figure 11.** Annual average initiation frequency of MCSs in IMERG (a), ICON (b), and their difference. Ratio of MCS precipitation compared to total precipitation averaged over the simulation period from IMERG (d), ICON (e), and their difference (f). Monthly mean MCS frequency over land (green) and ocean (blue) in the northern hemisphere (g;  $>20^\circ$ ), the tropics (h;  $\leq \pm 20^\circ$ ), and the Southern Hemisphere (i;  $<20^\circ$ ). IMERG results are shown with solid lines, while dashed lines show ICON results. The thick line represents the median frequency, while the contours indicate the maximum and minimum spreads over the four years.

404 land-based MCSs. Finally, modeled MCS durations are too short (2–4 hours median difference), with larger differences over  
 405 land than over ocean (Fig. 12d).

406 To compare the temporal evolution of MCSs, we differentiate between short-lived (4-9 hours) and long-lived ( $>14$  hours)  
 407 tropical MCSs, given lifetime-dependent model biases. The growth and decay of MCS cloud shields are well simulated for  
 408 oceanic and land-based tropical MCSs (Fig. 12e,f). However, long-lived storms do not grow fast enough and reach a peak size  
 409 that is about 20–30 % too small. On the other side, long-lived storms feature more accurate movement speeds while small  
 410 storms move about 20 % too fast (Fig. 12g,h).

411 Mean MCS precipitation starts high during the initiation phase of MCSs and steadily decreases during their lifetime (Fig. 12i,j).  
 412 This is because most MCSs start from a burst of small-scale convection and develop stratiform precipitation areas as they grow  
 413 upscale until the convective areas die off in the decaying phase, resulting in mostly stratiform precipitation (e.g., Mapes et al.,  
 414 2006). ICON simulates mean precipitation within  $\pm 20\%$  of observed values during the growth phase, with the exception of  
 415 land-based long-lived systems, which show a high difference of up to 40 %. Long-lived MCSs maintain high mean precipita-  
 416 tion rates during the growth phase of the storm (especially over tropical land), while simulated MCSs show a decline in mean

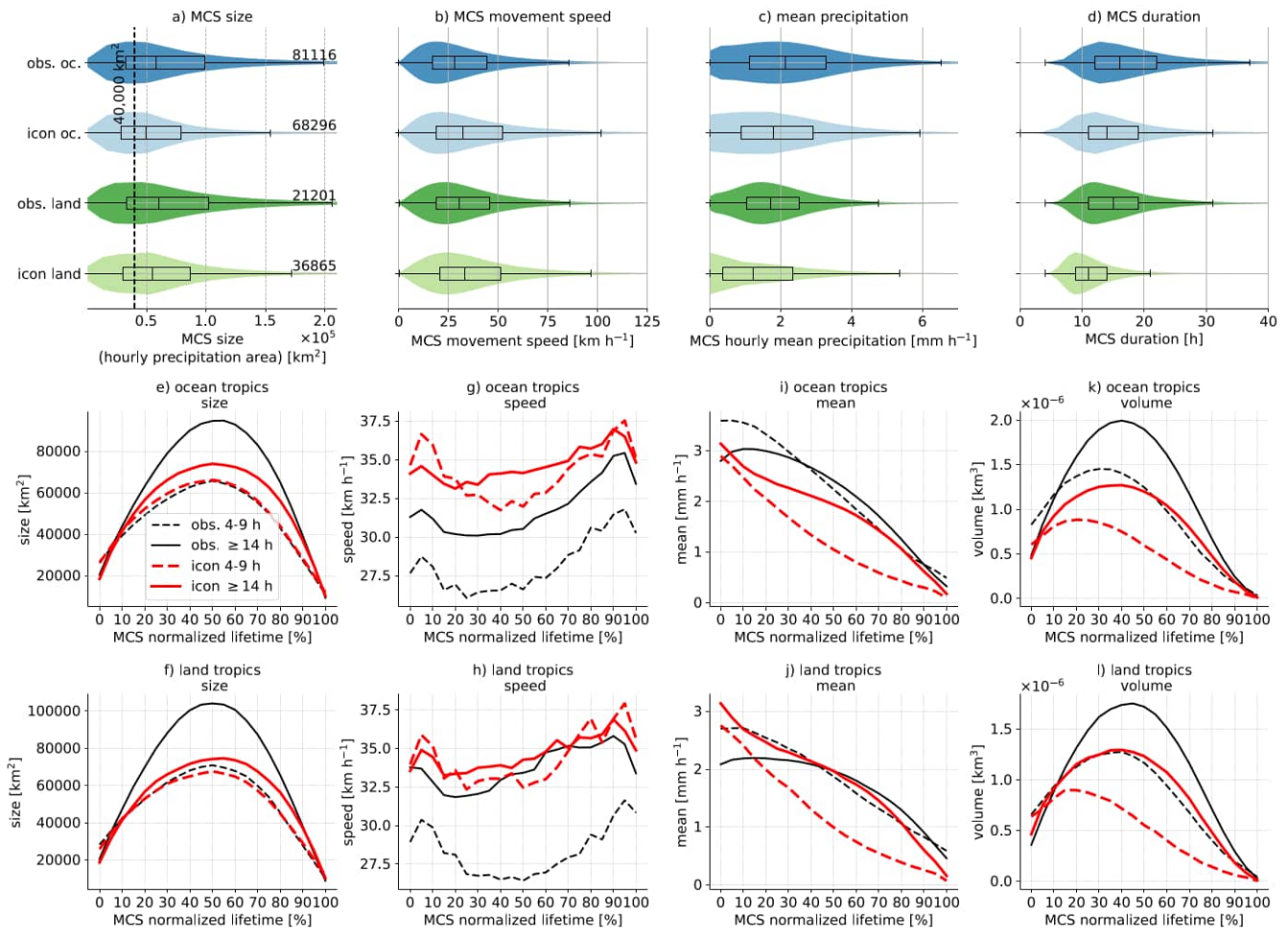


**Figure 12.** Violin and box-whisker plots for the distribution of tropical MCS sizes (a), speed (b), mean precipitation (c), and duration (d). The numbers right to the violins in (a) show the number of MCSs in each distribution. The lower panels show the normalized median evolution of short-lived (4-9 hours; dashed) and long-lived ( $\geq 14$  hours; solid) MCSs in GPM observations (black lines) and in ICON (red lines). The middle panels show results for tropical oceans while the lower panel shows tropical land regions.

417 precipitation even early on during their lifetime. This results in simulated mean MCS precipitation becoming increasingly  
 418 low-biased over the life cycle of storms ending at low differences of up to -60% during the decaying phase. This indicates  
 419 difficulties in simulating MCS stratiform precipitation, which is a common issue in many km-scale models (e.g., Prein et al.,  
 420 2023a; Zhang et al., 2024).

421 Finally, the combined differences in mean precipitation rates and MCS size are affecting the differences in MCS precipitation  
 422 volume, which is better simulated during the growth phase but becomes increasingly negatively biased over their lifetime,  
 423 especially for short-lived systems (Fig. 12k,l). The dominant driver of this bias is the low mean precipitation difference for

424 short-lived systems, as well as the low size difference for long-lived storms. We refrain from analyzing differences in the  
425 development of heavy precipitation rates due to the deficiencies in capturing these in GPM-IMERG (see Fig. 4.)

### 426 **3.8 Precipitating cloud characteristics**

427 We found some of the largest model wet biases in tropical ocean ITCZ precipitation (Fig. 3). At the same time, MCSs are  
428 too infrequent in this region. To better understand the causes of this bias we also tracked smaller precipitating cloud systems  
429 that have cold cloud tops in addition to MCSs (see section 2.3.1 and Fig. 13a–c). As previous studies have shown, cloud sizes  
430 (i.e., cold cloud top areas) follow a power-law frequency distribution (e.g., Savre and Craig, 2023). Observations show that  
431 cold cloud shields that exceed our MCS threshold ( $>40,000 \text{ km}^2$ ) contribute the most to tropical precipitation with a maximum  
432 contribution from clouds with  $\sim 75,000 \text{ km}^2$  (Fig. 13a). This maximum is shifted towards smaller cloud sizes and lower volumes  
433 in ICON (Fig. 13b) with a low contribution bias for large clouds and an overestimation from small clouds (Fig. 13c). Not visible  
434 in Fig. 13 are the low-frequency biases in MCSs over land and ocean, and in non-MCS precipitating cold clouds over land  
435 (Fig. S9), since only normalized distributions are shown. These results are broadly consistent with Segura and Hohenegger  
436 (2024), who showed that a large fraction of tropical precipitation originates from congestus clouds. GPM-IMERGv7 is not  
437 well suited to robustly quantify precipitation specifically from shallow or congestus clouds due to deficiencies in detecting  
438 precipitation from warm rain clouds (North et al., 2022; Huffman et al., 2023).

439 A key question is: which clouds cause the excess simulated precipitation in the tropics if deep convective clouds are too  
440 infrequent and too small? Fig. 13d–f show that in observations, most tropical precipitation originates beneath cold cloud tops,  
441 while ICON simulations have a too large fraction of rainfall coming from warm clouds. This issue is particularly evident  
442 in tropical land and ocean regions, but is also evident to a lesser extent in the Northern and Southern Hemispheres (Fig. S9  
443 and Fig. S10). Excess precipitation from clouds with warm cloud tops indicates overly active warm-cloud processes, too slow  
444 glaciation in tropical clouds in the ICON microphysics scheme, or errors in GPM-IMERGv7 in capturing warm rain. This is  
445 consistent with the underestimated surface shortwave radiation over tropical oceans (Fig. 2c) that could be caused by overly  
446 reflective or overly abundant water clouds.

### 447 **3.9 Drivers of heavy precipitation**

448 The output from the MOAAP algorithm allows us to analyze the interactions among atmospheric phenomena in creating hourly  
449 heavy precipitation events in observations and in the ICON model (Fig. 14). We decided to exclude equatorial waves and fronts  
450 from the analysis in Fig. 14a–f since equatorial waves dominate tropical heavy precipitation statistics due to their large size,  
451 and including them obscures details from smaller-scale phenomena (Fig. S12). We decided to exclude fronts because they are  
452 more frequent in ICON, likely due to its higher model resolution, which allows sharper gradients to be simulated. Results  
453 including fronts and equatorial waves are shown in Fig. S12.

454 ICON can effectively simulate the processes that cause extreme precipitation across different climate regions, though it  
455 has some notable deficiencies. In observations, MCSs are more often the most frequent producers of heavy precipitation in  
456 tropical and subtropical ocean regions (Fig. 14a,b). This agrees with our previous analysis, which showed low-frequency and

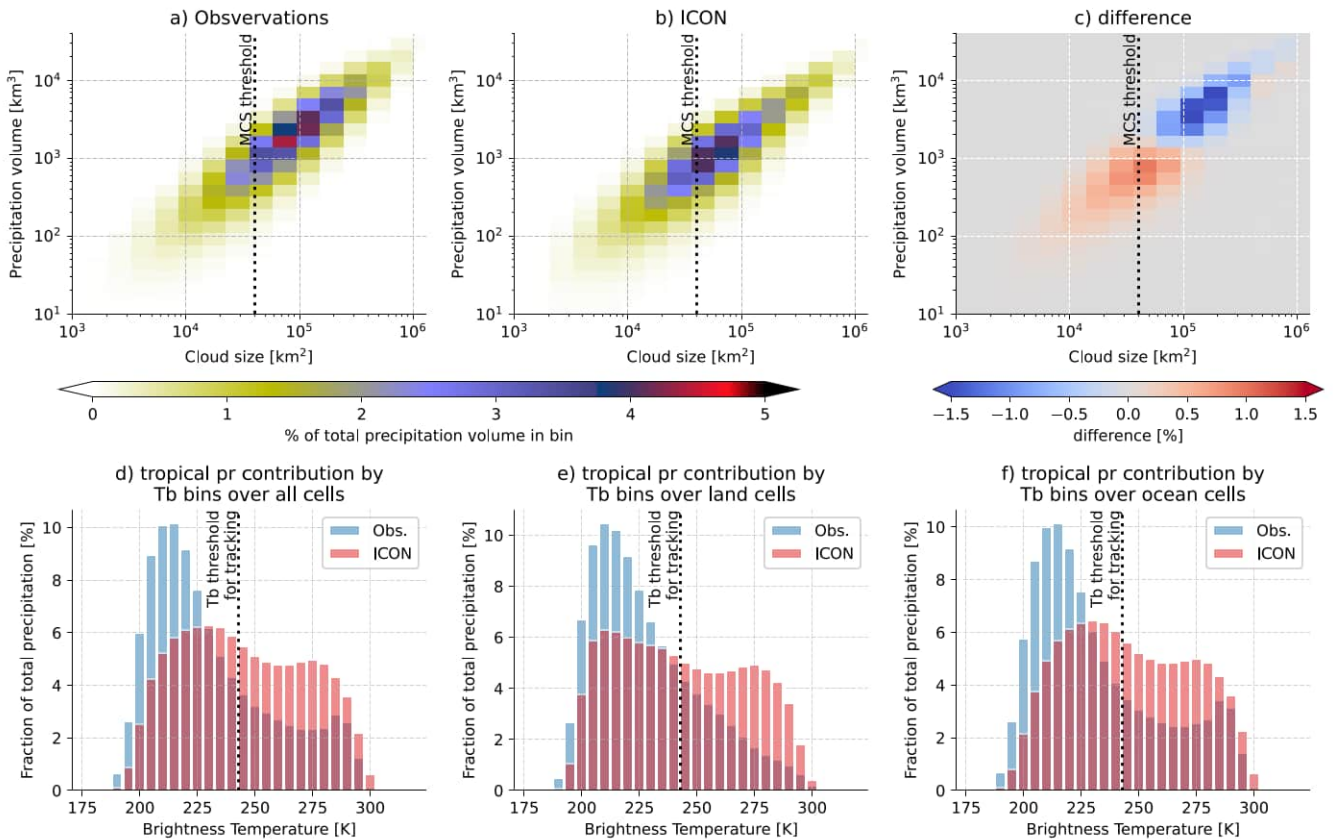


**Figure 13.** Relative contribution of tropical (latitude  $< \pm 20^\circ$ ) total precipitation from storms with cold cloud shields (Tb < 243 K) as a function of cloud shield size and precipitation volume under the cloud from observations (a), ICON (b), and their difference (c). The vertical dashed line shows the cloud shield threshold used for MCS classification. The fraction of total precipitation conditioned on Tb over the tropics (d), tropical land (e), and tropical ocean (f). The vertical dashed line shows the Tb threshold used for cold cloud identification.

457 size differences in simulated MCSs. In contrast, simulated MCSs are more dominant over tropical and subtropical land regions,  
 458 where observations highlight non-MCS cold clouds as most important. At the same time, moisture streams (areas of low-level  
 459 strong and coherent horizontal moisture transport) are frequently more relevant in ICON than in observations, particularly in  
 460 subtropical ocean regions.

461 Fig. 14g–i show frequency statistics that visualize how often a phenomenon was co-located with hourly heavy precipitation  
 462 in the Northern European (NEU), Southeast South America (SES), and the Equatorial Pacific Ocean (EPO) region. In the high-  
 463 latitude NEU region, observations and ICON agree that surface cyclones and mid-level cyclones are the most frequent drivers  
 464 with secondary contributions from jet streams and moisture streams (Fig. 14g). ICON features more heavy precipitation events  
 465 from non-MCS clouds than observed and a larger contribution of frontal systems. Cut-off lows are less frequently involved in  
 466 simulated heavy precipitation events than in observations.

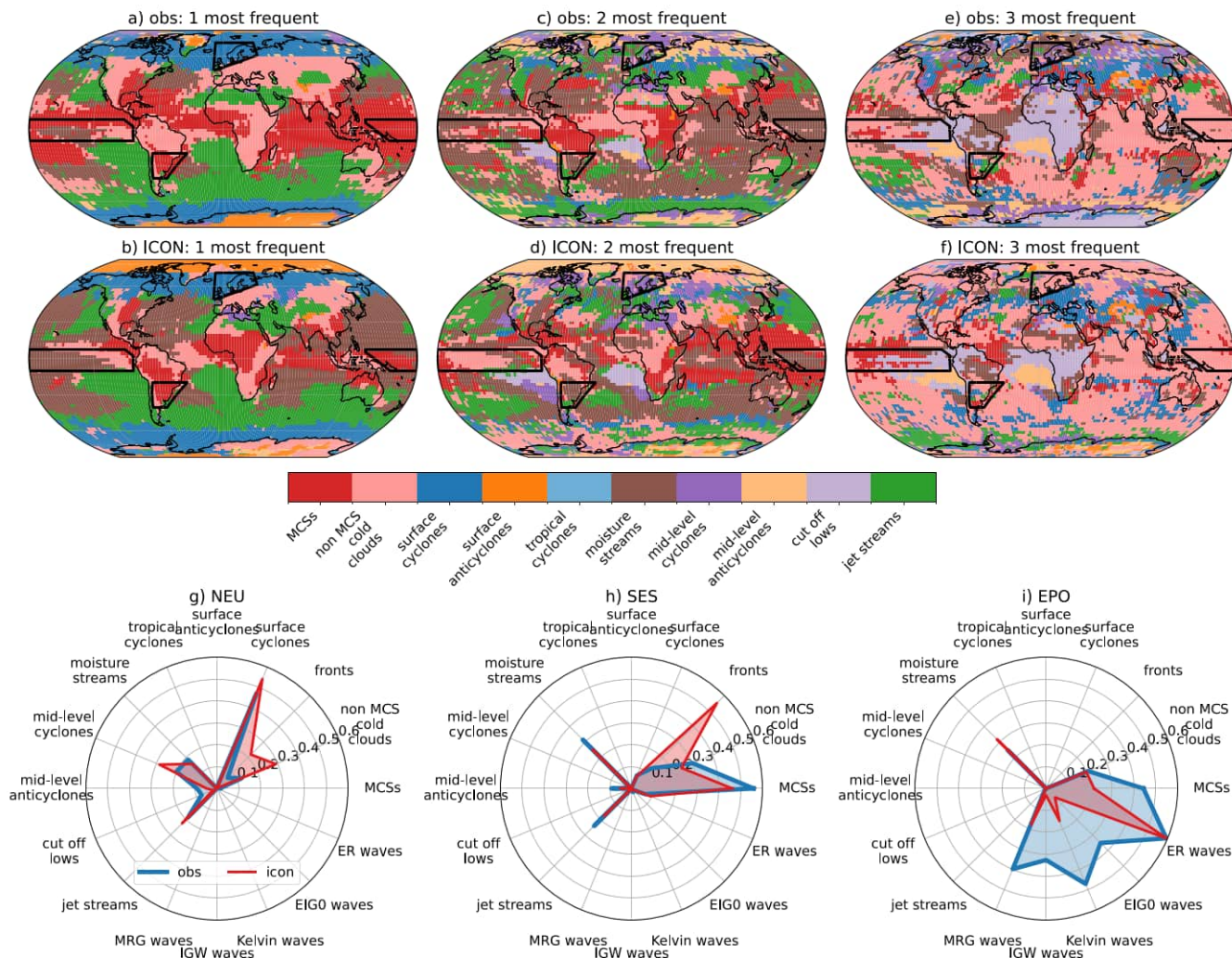


**Figure 14.** The most frequent (a,b), second most frequent (c,d), and third most frequent (e,f) atmospheric phenomena identified by the MOAAP algorithm that is co-located during the top 20 hourly precipitation events in the evaluation period. Observed/ICON results are shown in the top/middle panel. The data were upscaled to a  $2.5^\circ$  grid to reduce the signal-to-noise ratio. The same data is shown in panel (g–i) as the fractional frequency of the phenomenon in the Northern European (NEU), Southeast South America (SES), and Equatorial Pacific Ocean (EPO) regions (these regions are highlighted in the maps in (a–f)). A value of 0.5 means that 50% of all grid cells in a region had the corresponding phenomena co-located during a heavy precipitation event.

467 In the SES region, ICON agrees with observations that MCSs and non-MCS clouds are the dominant heavy precipitation-  
 468 producing phenomena (Fig. 14h). ICON also captures the importance of moisture streams and jet streams well, while frontal  
 469 involvement is much higher than in ERA5.

470 We find a relatively poor agreement in the tropical EPO region (Fig. 14i) where ICON substantially underestimates the  
471 importance of MCSs and all equatorial waves except for Equatorial Rossby waves, in agreement with previously shown re-  
472 sults. However, ICON can capture the importance of non-MCS cold clouds and moisture streams in the production of heavy  
473 precipitation.

#### 474 **4 Summary and Conclusion**

475 We present results from the first multi-year (April 2020–March 2024), global prescribed SST km-scale simulation performed  
476 with the GT4Py GPU-refactored ICON model (Dipankar et al., 2026) at a horizontal grid spacing of 2.5 km and 120 vertical  
477 levels. This experiment, conducted within the EXCLAIM project, represents a major milestone toward bridging the long-  
478 standing divide between numerical weather prediction (NWP) and climate modeling (Randall and Emanuel, 2024), using a  
479 model configuration based on operational forecasting without empirical tuning. By explicitly resolving deep convection, oro-  
480 graphic drag, mesoscale circulations, and local land heterogeneity globally, the model enables the consistent study of weather  
481 and climate processes within a unified physical framework.

482 We conducted a comprehensive evaluation using satellite, reanalysis, and in-situ observations to assess the fidelity of the  
483 simulation of atmospheric phenomena at scales ranging from global to local. The following main points summarize our study:

- 484 – The ICON model reproduces observed large-scale patterns of temperature, precipitation, and surface energy fluxes with  
485 high fidelity, showing good agreement with reanalysis, satellite, and in situ observations, although biases, such as over-  
486 estimation of sensible heat fluxes over land during the warm season, persist. Importantly, the model can realistically  
487 simulate the spatial pattern of tropical precipitation with a single ITCZ. However, there is an overestimation of tropical  
488 oceanic clouds (up to -40 % in incoming shortwave radiation at the surface) and precipitation (up to 50 %) and cold biases  
489 in polar regions (more than -3 °C) during winter. Additionally, warm biases over mid-latitude continents during the warm  
490 season are related to too much incoming solar radiation, an underestimation in latent heat fluxes, and an overestimation  
491 of sensible heat fluxes.
- 492 – Explicitly resolving convection yields a realistic convective diurnal cycle and an excellent representation of the hourly  
493 rainfall probability density distribution, including extremes. Still, some land regions, such as those over southern Africa,  
494 Australia, and parts of the Amazon basin, feature a diurnal precipitation peak that is too early. Importantly, model  
495 analyses that focus on the intensity or frequency of hourly precipitation should use in-situ observation records where  
496 possible, since these precipitation characteristics are not well captured in GPM-IMERG-v7 and reanalysis products, as  
497 we show here and in previous work (e.g., Dominguez et al., 2024).
- 498 – Near-surface winds and tropical cyclone statistics are generally well simulated, but maximum wind speeds are underes-  
499 timated by  $\sim 20\%$ . Tropical cyclone frequencies are well captured, except in the North Atlantic basin, where low biases  
500 are observed, similar to other high-resolution climate model simulations (Roberts et al., 2020).

- 501 – Spatial initiation patterns of MCSs are realistic, but ICON underestimates oceanic MCS frequencies (especially outside  
502 DJF) and overestimates tropical land MCSs. Simulated systems are smaller, slightly too fast, and too short-lived, resulting  
503 in an underestimation of MCS precipitation over oceans and an overestimation over some tropical land areas. The low  
504 bias in tropical MCS precipitation and the underestimation of MCS size are common among km-scale global models  
505 (Feng et al., 2025). The low-frequency bias in long-lived, large MCSs contributes to the earlier peak timing in the  
506 convective diurnal cycle.
- 507 – Since both precipitation from MCS and non-MCS cold clouds is underestimated over tropical ocean regions, it is unclear  
508 which clouds are causing the oceanic wet tropical precipitation difference in ICON. The primary cause is larger simulated  
509 rainfall from shallow and mid-level clouds (e.g., cumulus congestus) in the model. The reason for these differences is  
510 unclear, but an overactive warm-rain process in the model and deficiencies in warm-rain detection in GPM-IMERG-v7  
511 might contribute.
- 512 – The frequency and amplitude of all equatorial waves except for Rossby waves are underestimated. This is consistent with  
513 the underestimation of MCSs and the overestimation of precipitation from shallow clouds in the tropics since equatorial  
514 waves are frequently coupled to deep convection (Kiladis et al., 2009; Prein et al., 2023b). Km-scale global models tend  
515 to capture equatorial Rossby waves well since their dynamics are more strongly controlled by large-scale vorticity gra-  
516 dients rather than the details of convective heating, although column water vapor also contributes (Yasunaga and Mapes,  
517 2012; Yasunaga et al., 2019; Nakamura and Takayabu, 2022). Previous global km-scale modeling studies have shown  
518 that uncoupled models can capture convective-coupled equatorial waves (e.g., Judt and Rios-Berrios, 2021; Takasuka  
519 et al., 2024a; Ortega et al., 2026). The biases presented here might also stem in part from a misrepresentation of ther-  
520 modynamic–convection coupling, which can strongly influence convective organization and its coupling to larger-scale  
521 tropical variability (Takasuka et al., 2026). Additionally, ocean-atmosphere interactions are important for simulating  
522 connectively coupled equatorial waves, which our forced SST setup does not capture (e.g., DeMott et al., 2015).
- 523 – An object-based evaluation using the MOAAP feature tracker (Prein et al., 2023b) reveals that ICON realistically cap-  
524 tures the main meteorological drivers of heavy hourly precipitation, including cyclones, MCSs, and moisture streams. We  
525 consistently find deficiencies in simulating heavy rainfall associated with tropical oceanic MCSs and equatorial waves.

526 In summary, the EXCLAIM 2.5 km global ICON simulation provides a unique benchmark for studying global hydroclimatic  
527 extremes and mesoscale dynamics. It will serve as a contribution to the DYAMOND-III intercomparison initiative (Takasuka  
528 et al., 2024b), allowing for comparison with an ensemble of km-scale global models. The simulation offers novel insight into  
529 the interplay between different modes of convection and large-scale circulation. Current ICON developments within the EX-  
530 CLAIM project aim to optimize the code for faster runtime and implement ocean-atmosphere coupling at km-scales (Dipankar  
531 et al., 2026). This framework also provides a basis for follow-up studies investigating how mesoscale processes, such as con-  
532 vective outbreaks, feed back onto and modify the larger-scale circulation. Future studies will also focus on longer integration  
533 periods, as four years are insufficient to capture climate variability.

534 While notable challenges remain in representing tropical variability, mesoscale convective organization, and land-atmosphere  
535 coupling, the demonstrated capability of our simulation and other km-scale global modeling efforts establishes a new founda-  
536 tion for next-generation Earth system modeling and the transition toward truly unified weather–climate simulations.

537 *Code and data availability.* The global 2.5 km ICON simulation was produced within the EXCLAIM project following the DYAMOND-III  
538 protocol (Prein, 2026).

539 The ICON model version used in this study corresponds to ICON-EXCLAIM v0.2.0. The complete model source code, including the  
540 EXCLAIM extensions, is publicly archived at Zenodo (Dipankar, 2025): <https://doi.org/10.5281/zenodo.17255275>

541 The configuration files, namelists, and run scripts used to perform the global 2.5 km simulation are archived separately at Zenodo: <https://doi.org/10.5281/zenodo.17250248>

542  
543 ICON global 2.5 km simulation and analysis data can be accessed from Figshare: <https://doi.org/10.6084/m9.figshare.31341982>.

544 The analysis and visualization code used to process the model output and observational datasets, and to generate all figures in this  
545 manuscript, is archived on Zenodo (Prein, 2025): <https://doi.org/10.5281/zenodo.18648539>.

546 ERA5 reanalysis data were obtained from the Copernicus Climate Data Store (Hersbach et al., 2020): Copernicus Climate Change Service  
547 Climate Data Store. <https://doi.org/10.24381/cds.adbb2d47>.

548 NOAA Interpolated Outgoing Longwave Radiation (OLR) data were obtained from NOAA Physical Sciences Laboratory (PSL), dataset  
549 “NOAA Interpolated OLR” (accessed 2026.02.15): <https://psl.noaa.gov/data/gridded/data.olrcdr.interp.html>. The interpolation method is  
550 described by Liebmann and Smith (1996).

551 GPM IMERG precipitation data were obtained from the NASA Goddard Earth Sciences Data and Information Services Center (Huffman  
552 et al., 2020): <https://doi.org/10.5067/GPM/IMERG/3B-HH/07>; [https://disc.gsfc.nasa.gov/datasets/GPM\\_3IMERGHH\\_07/summary](https://disc.gsfc.nasa.gov/datasets/GPM_3IMERGHH_07/summary).

553 Merged infrared brightness temperature data were obtained from the NOAA Climate Prediction Center merged IR dataset archive: <https://doi.org/10.5067/P4HZB9N27EKU>.

554  
555 HadISD station observations were obtained from the Met Office Hadley Centre archive (Dunn et al., 2016): <https://www.metoffice.gov.uk/hadobs/hadisd/>.

556  
557 FLUXNET2015 surface flux data were obtained from the FLUXNET data archive (Pastorello et al., 2020): <https://doi.org/10.18140/FLX/1440160>.

558  
559 AmeriFlux surface flux data were obtained from the AmeriFlux data archive: <https://ameriflux.lbl.gov/data/>.

560 IBTrACS tropical cyclone data were obtained from NOAA National Centers for Environmental Information (Gahtan et al., 2024): <https://doi.org/10.25921/82ty-9e16>; <https://www.ncei.noaa.gov/products/international-best-track-archive>.

561  
562 EWEMBI surface radiation data were obtained from the ISIMIP data archive (Lange, 2018): [https://www.isimip.org/gettingstarted/inpu](https://www.isimip.org/gettingstarted/input-data-bias-adjustment/details/27/)  
563 [t-data-bias-adjustment/details/27/](https://www.isimip.org/gettingstarted/input-data-bias-adjustment/details/27/).

564 *Author contributions.* AFP designed, conceptualized, performed most of the analyses, and wrote the first draft of the manuscript. PP ran the  
565 ICON simulations and archived the data with support from CZ. ML performed the surface flux analyses, and MR performed the Wheeler

566 and Kiladis analysis. AD, ML, and AJ supported the development and configuration of the applied ICON model. All authors contributed to  
567 the writing of the paper.

568 *Competing interests.* We do not have any competing interests.

569 *Acknowledgements.* This work was supported by a grant from the Swiss National Supercomputing Centre (CSCS) under the EXCLAIM  
570 project on Alps. The authors thank the NOAA Physical Sciences Laboratory (PSL), Boulder, Colorado, USA, for providing the Interpolated  
571 Outgoing Longwave Radiation (OLR) dataset, available at <https://psl.noaa.gov>. ERA5 reanalysis data were obtained from the Copernicus  
572 Climate Change Service (C3S) Climate Data Store. The GPM IMERG data were provided by the NASA/Goddard Space Flight Center's  
573 Global Precipitation Measurement and PPS, which develop and compute the GPM IMERG as a contribution to GPM, and archived at  
574 the NASA GES DISC. Merged infrared brightness temperature data were provided by NASA and NOAA. We acknowledge the UK Met  
575 Office for HadISD station observations, the FLUXNET and AmeriFlux networks and their contributing site investigators, NOAA/NCEI for  
576 IBTrACS tropical cyclone data, and ISIMIP for providing the EWEMBI surface radiation dataset. We used Grammarly and ChatGPT to  
577 support the writing of this manuscript.

## 578 References

- 579 EartH2Observe, WFDEI and ERA-Interim data Merged and Bias-corrected for ISIMIP (EWEMBI), author=Lange, Stefan, (No Title), 2016.
- 580 Ahlgrimm, M. and Forbes, R.: The impact of low clouds on surface shortwave radiation in the ECMWF model, *Monthly Weather Review*,  
581 140, 3783–3794, 2012.
- 582 Argüeso, D., Di Luca, A., and Evans, J. P.: Precipitation over urban areas in the western Maritime Continent using a convection-permitting  
583 model, *Climate dynamics*, 47, 1143–1159, 2016.
- 584 Asensio, H., Messmer, M., Lüthi, D., and Osterried, K.: External Parameters for Numerical Weather Prediction and Climate Ap-  
585 plication EXTPAR v5\_0, User and Implementation Guide. Available online: [http://www.cosmo-model.org/content/support/soft-](http://www.cosmo-model.org/content/support/software/ethz/EXTPAR_user_and_implementation_manual_202003.pdf)  
586 [ware/ethz/EXTPAR\\_user\\_and\\_implementation\\_](http://www.cosmo-model.org/content/support/software/ethz/EXTPAR_user_and_implementation_manual_202003.pdf)  
manual\_202003.pdf (accessed on 16 November 2018), 2020.
- 587 Ban, N., Schmidli, J., and Schär, C.: Evaluation of the convection-resolving regional climate modeling approach in decade-long simulations,  
588 *Journal of Geophysical Research: Atmospheres*, 119, 7889–7907, 2014.
- 589 Ban, N., Caillaud, C., Coppola, E., Pichelli, E., Sobolowski, S., Adinolfi, M., Ahrens, B., Alias, A., Anders, I., Bastin, S., et al.: The first  
590 multi-model ensemble of regional climate simulations at kilometer-scale resolution, part I: evaluation of precipitation, *Climate Dynamics*,  
591 57, 275–302, 2021.
- 592 Barlage, M., Chen, F., Rasmussen, R., Zhang, Z., and Miguez-Macho, G.: The importance of scale-dependent groundwater processes in  
593 land-atmosphere interactions over the central United States, *Geophysical Research Letters*, 48, e2020GL092171, 2021.
- 594 Brown, A., Dowdy, A., and Lane, T. P.: Convection-permitting climate model representation of severe convective wind gusts and future  
595 changes in southeastern Australia, *Natural Hazards and Earth System Sciences*, 24, 3225–3243, 2024.
- 596 Chu, H., Christianson, D. S., Cheah, Y.-W., Pastorello, G., O’Brien, F., Geden, J., Ngo, S.-T., Hollowgrass, R., Leibowitz, K., Beekwilder,  
597 N. F., et al.: AmeriFlux BASE data pipeline to support network growth and data sharing, *Scientific Data*, 10, 614, 2023.
- 598 Clark, P., Roberts, N., Lean, H., Ballard, S. P., and Charlton-Perez, C.: Convection-permitting models: A step-change in rainfall forecasting,  
599 *Meteorological Applications*, 23, 165–181, 2016.
- 600 Dee, D. P., Uppala, S., Simmons, A. J., Berrisford, P., Poli, P., Kobayashi, S., Andrae, U., Balmaseda, M., Balsamo, G., Bauer, d. P., et al.: The  
601 ERA-Interim reanalysis: Configuration and performance of the data assimilation system, *Quarterly Journal of the royal meteorological*  
602 *society*, 137, 553–597, <https://doi.org/https://doi.org/10.1002/qj.828>, 2011.
- 603 DeMott, C. A., Klingaman, N. P., and Woolnough, S. J.: Atmosphere-ocean coupled processes in the Madden-Julian oscillation, *Reviews of*  
604 *Geophysics*, 53, 1099–1154, 2015.
- 605 Deser, C., Phillips, A., Bourdette, V., and Teng, H.: Uncertainty in climate change projections: the role of internal variability, *Climate*  
606 *dynamics*, 38, 527–546, 2012.
- 607 Dipankar, A.: EXCLAIM use cases, <https://doi.org/10.5281/zenodo.17250248>, 2025.
- 608 Dipankar, A., Bianco, M., Bukenberger, M., Ehrenguber, T., Farabullini, N., Gopal, A., Hupp, D., Jocksch, A., Kellerhals, S., Kroll, C. A.,  
609 Lapillonne, X., Leclair, M., Luz, M., Müller, C., Ong, C. R., Osuna, C., Pothapakula, P., Röthlin, M., Sawyer, W., Serafini, G., Vogt, H.,  
610 Weber, B., and Schulthess, T.: Toward Exascale Climate Modelling: A Python DSL Approach to ICON’s (Icosahedral Non-hydrostatic)  
611 Dynamical Core (icon-exclaim v0.2.0), *EGUsphere*, 2025, 1–26, <https://doi.org/10.5194/egusphere-2025-4808>, 2025.
- 612 Dipankar, A., Bianco, M., Bukenberger, M., Ehrenguber, T., Farabullini, N., Fuhrer, O., Gopal, A., Hupp, D., Jocksch, A., Kellerhals, S.,  
613 Kroll, C. A., Lapillonne, X., Leclair, M., Luz, M., Müller, C., Ong, C. R., Osuna, C., Pothapakula, P., Prein, A., Röthlin, M., Sawyer,  
614 W., Schär, C., Schemm, S., Serafini, G., Vogt, H., Weber, B., Wills, R. C. J., Gruber, N., and Schulthess, T. C.: Toward exascale climate

615 modelling: a python DSL approach to ICON's (icosahedral non-hydrostatic) dynamical core (icon-exclaim v0.2.0), *Geoscientific Model*  
616 *Development*, 19, 713–729, <https://doi.org/10.5194/gmd-19-713-2026>, 2026.

617 Dominguez, F., Rasmussen, R., Liu, C., Ikeda, K., Prein, A., Varble, A., Arias, P. A., Bacmeister, J., Bettolli, M. L., Callaghan, P., et al.:  
618 Advancing South American water and climate science through multidecadal convection-permitting modeling, *Bulletin of the American*  
619 *Meteorological Society*, 105, E32–E44, 2024.

620 Donahue, A. S., Caldwell, P. M., Bertagna, L., Beydoun, H., Bogenschutz, P. A., Bradley, A., Clevenger, T. C., Foucar, J., Golaz, C., Guba,  
621 O., et al.: To exascale and beyond—The Simple Cloud-Resolving E3SM Atmosphere Model (SCREAM), a performance portable global  
622 atmosphere model for cloud-resolving scales, *Journal of Advances in Modeling Earth Systems*, 16, e2024MS004314, 2024.

623 Donat, M. G., Lowry, A. L., Alexander, L. V., O’Gorman, P. A., and Maher, N.: More extreme precipitation in the world’s dry and wet  
624 regions, *Nature Climate Change*, 6, 508–513, 2016.

625 Dunn, Robert J. H.: HadISD.3.4.0: Product User Guide, Met Office Hadley Centre, Exeter, UK, <https://hadleyserver.metoffice.gov.uk/hadis>  
626 [d/hadisd\\_v340\\_2023f\\_product\\_user\\_guide.pdf](https://hadleyserver.metoffice.gov.uk/hadis), version 3.4.0 (2023f) of the HadISD dataset, updated 12 Jan 2024., 2024.

627 Dunn, R. J., Willett, K. M., Parker, D. E., and Mitchell, L.: Expanding HadISD: Quality-controlled, sub-daily station data from 1931,  
628 *Geoscientific Instrumentation, Methods and Data Systems*, 5, 473–491, 2016.

629 Feng, Z., Prein, A. F., Kukulies, J., Fiolleau, T., Jones, W. K., Maybee, B., Moon, Z. L., Núñez Ocasio, K. M., Dong, W., Molina, M. J., et al.:  
630 Mesoscale convective systems tracking method intercomparison (MCSMIP): Application to DYAMOND global km-scale simulations,  
631 *Journal of Geophysical Research: Atmospheres*, 130, e2024JD042204, 2025.

632 Gahtan, J., Knapp, K. R., Schreck, C. J. I., Diamond, H. J., Kossin, J. P., and Kruk, M. C.: International Best Track Archive for Climate  
633 Stewardship (IBTrACS) Project, Version 4.01, NOAA National Centers for Environmental Information, <https://doi.org/10.25921/82ty->  
634 [9e16](https://doi.org/10.25921/82ty-), 2024.

635 Gentry, M. S. and Lackmann, G. M.: Sensitivity of simulated tropical cyclone structure and intensity to horizontal resolution, *Monthly*  
636 *Weather Review*, 138, 688–704, 2010.

637 Giorgetta, M. A., Sawyer, W., Lapillonne, X., Adamidis, P., Alexeev, D., Clément, V., Dietlicher, R., Engels, J. F., Esch, M., Franke, H.,  
638 et al.: The ICON-A model for direct QBO simulations on GPUs (version icon-cscs: baf28a514), *Geoscientific Model Development*, 15,  
639 6985–7016, 2022.

640 Giorgi, F. and Gutowski Jr, W. J.: Regional dynamical downscaling and the CORDEX initiative, *Annual review of environment and resources*,  
641 40, 467–490, 2015.

642 Giorgi, F., Jones, C., Asrar, G. R., et al.: Addressing climate information needs at the regional level: the CORDEX framework, *World*  
643 *Meteorological Organization (WMO) Bulletin*, 58, 175, 2009.

644 Grasselt, R., Schuttemeyer, D., Warrach-Sagi, K., Ament, F., and Simmer, C.: Validation of TERRA-ML with discharge measurements,  
645 *Meteorologische Zeitschrift*, 17, 763, 2008.

646 Guilloteau, C. and Foufoula-Georgiou, E.: Multiscale evaluation of satellite precipitation products: Effective resolution of IMERG, in: *Satel-*  
647 *lite Precipitation Measurement: Volume 2*, pp. 533–558, Springer, 2020.

648 Gutmann, E. D., Rasmussen, R. M., Liu, C., Ikeda, K., Bruyere, C. L., Done, J. M., Garrè, L., Friis-Hansen, P., and Veldore, V.: Changes in  
649 hurricanes from a 13-yr convection-permitting pseudo-global warming simulation, *Journal of Climate*, 31, 3643–3657, 2018.

650 Hayden, L. and Liu, C.: Differences in the diurnal variation of precipitation estimated by spaceborne radar, passive microwave radiometer,  
651 and IMERG, *Journal of Geophysical Research: Atmospheres*, 126, e2020JD033020, 2021.

652 He, J., Hong, L., Shao, C., and Tang, W.: Global evaluation of simulated surface shortwave radiation in CMIP6 models, *Atmospheric*  
653 *Research*, 292, 106 896, 2023.

654 Hersbach, H., Bell, B., Berrisford, P., Hirahara, S., Horányi, A., Muñoz-Sabater, J., Nicolas, J., Peubey, C., Radu, R., Schepers, D., et al.:  
655 The ERA5 global reanalysis, *Quarterly journal of the royal meteorological society*, 146, 1999–2049, 2020.

656 Hohenegger, C., Brockhaus, P., Bretherton, C. S., and Schär, C.: The soil moisture–precipitation feedback in simulations with explicit and  
657 parameterized convection, *Journal of Climate*, 22, 5003–5020, 2009.

658 Hohenegger, C., Kornbluh, L., Klocke, D., Becker, T., Cioni, G., Engels, J. F., Schulzweida, U., and Stevens, B.: Climate statistics in global  
659 simulations of the atmosphere, from 80 to 2.5 km grid spacing, *Journal of the Meteorological Society of Japan. Ser. II*, 98, 73–91, 2020.

660 Hohenegger, C., Korn, P., Linardakis, L., Redler, R., Schnur, R., Adamidis, P., Bao, J., Bastin, S., Behraves, M., Bergemann, M., et al.:  
661 ICON-Sapphire: simulating the components of the Earth system and their interactions at kilometer and subkilometer scales, *Geoscientific*  
662 *Model Development*, 16, 779–811, 2023.

663 Holloway, C., Woolnough, S., and Lister, G.: Precipitation distributions for explicit versus parametrized convection in a large-domain high-  
664 resolution tropical case study, *Quarterly Journal of the Royal Meteorological Society*, 138, 1692–1708, 2012.

665 Huffman, G. J., Bolvin, D. T., Braithwaite, D., Hsu, K.-L., Joyce, R. J., Kidd, C., Nelkin, E. J., Sorooshian, S., Stocker, E. F., Tan, J.,  
666 et al.: Integrated multi-satellite retrievals for the global precipitation measurement (GPM) mission (IMERG), in: *Satellite precipitation*  
667 *measurement: Volume 1*, pp. 343–353, Springer, 2020.

668 Huffman, G. J., Bolvin, D. T., Joyce, R., Kelley, O. A., Nelkin, E. J., Tan, J., Watters, D. C., and West, B. J.: Integrated Multi-satellitE  
669 Retrievals for GPM (IMERG) Technical Documentation, NASA Goddard Space Flight Center, [https://gpm.nasa.gov/sites/default/files/2023-07/IMERG\\_TechnicalDocumentation\\_final\\_230713.pdf](https://gpm.nasa.gov/sites/default/files/2023-07/IMERG_TechnicalDocumentation_final_230713.pdf), version 07, dated 13 July 2023, 2023.

671 Ikeda, K., Rasmussen, R., Liu, C., Newman, A., Chen, F., Barlage, M., Gutmann, E., Dudhia, J., Dai, A., Luce, C., et al.: Snowfall and  
672 snowpack in the Western US as captured by convection permitting climate simulations: Current climate and pseudo global warming future  
673 climate, *Climate Dynamics*, 57, 2191–2215, 2021.

674 IPCC: Climate Change 2023: Synthesis Report. Contribution of Working Groups I, II and III to the Sixth Assessment Report  
675 of the Intergovernmental Panel on Climate Change, Intergovernmental Panel on Climate Change (IPCC), Geneva, Switzerland,  
676 <https://doi.org/10.59327/IPCC/AR6-9789291691647>, 2023.

677 Janowiak, J., Joyce, B., and Xie, P.: NCEP/CPC L3 Half Hourly 4km global (60S–60N) Merged IR V1. Greenbelt, MD, Goddard Earth  
678 Sciences Data and Information Services Center (GES DISC), 2017.

679 Judt, F. and Rios-Berrios, R.: Resolved convection improves the representation of equatorial waves and tropical rainfall variability in a global  
680 nonhydrostatic model, *Geophysical Research Letters*, 48, e2021GL093 265, 2021.

681 Judt, F., Klocke, D., Rios-Berrios, R., Vanniere, B., Ziemer, F., Auger, L., Biercamp, J., Bretherton, C., Chen, X., Düben, P., et al.: Tropical  
682 cyclones in global storm-resolving models, *Journal of the Meteorological Society of Japan. Ser. II*, 99, 579–602, 2021.

683 Jung, H. and Knippertz, P.: Link between the time-space behavior of rainfall and 3d dynamical structures of equatorial waves in global  
684 convection-permitting simulations, *Geophysical Research Letters*, 50, e2022GL100 973, 2023.

685 Kendon, E., Prein, A. F., Senior, C., and Stirling, A.: Challenges and outlook for convection-permitting climate modelling, *Philosophical*  
686 *Transactions of the Royal Society A*, 379, 20190 547, 2021.

687 Kendon, E. J., Ban, N., Roberts, N. M., Fowler, H. J., Roberts, M. J., Chan, S. C., Evans, J. P., Fosse, G., and Wilkinson, J. M.: Do convection-  
688 permitting regional climate models improve projections of future precipitation change?, *Bulletin of the American Meteorological Society*,  
689 98, 79–93, 2017.

690 Kiladis, G. N., Wheeler, M. C., Haertel, P. T., Straub, K. H., and Roundy, P. E.: Convectively coupled equatorial waves, *Reviews of Geo-*  
691 *physics*, 47, 2009.

692 Kinne, S.: The MACv2 aerosol climatology, *Tellus B: Chemical and Physical Meteorology*, 71, 1–21, 2019.

693 Klocke, D., Frauen, C., Engels, J. F., Alexeev, D., Redler, R., Schnur, R., Haak, H., Kornbluch, L., Brüggemann, N., Chegini, F., et al.:  
694 Computing the Full Earth System at 1km Resolution, in: *Proceedings of the International Conference for High Performance Computing,*  
695 *Networking, Storage and Analysis*, pp. 125–136, 2025.

696 Knaff, J. A. and Zehr, R. M.: Reexamination of tropical cyclone wind–pressure relationships, *Weather and Forecasting*, 22, 71–88, 2007.

697 Knapp, K. R., Kruk, M. C., Levinson, D. H., Diamond, H. J., and Neumann, C. J.: The international best track archive for climate stewardship  
698 (IBTrACS) unifying tropical cyclone data, *Bulletin of the American Meteorological Society*, 91, 363–376, 2010.

699 Lange, S.: Bias correction of surface downwelling longwave and shortwave radiation for the EWEMBI dataset, *Earth System Dynamics*, 9,  
700 627–645, 2018.

701 Langendijk, G., Rechid, D., Sieck, K., and Jacob, D.: Added value of convection-permitting simulations for understanding future urban  
702 humidity extremes: case studies for Berlin and its surroundings, *Weather and Climate Extremes*, 33, 100–107, 2021.

703 Lee, J. and Hohenegger, C.: Weaker land–atmosphere coupling in global storm-resolving simulation, *Proceedings of the National Academy*  
704 *of Sciences*, 121, e2314265 121, 2024.

705 Liebmann, B. and Smith, C. A.: Description of a Complete (Interpolated) Outgoing Longwave Radiation Dataset, *Bulletin of the American*  
706 *Meteorological Society*, 77, 1275–1277, <http://www.jstor.org/stable/26233278>, 1996.

707 Liu, C., Ikeda, K., Rasmussen, R., Barlage, M., Newman, A. J., Prein, A. F., Chen, F., Chen, L., Clark, M., Dai, A., et al.: Continental-scale  
708 convection-permitting modeling of the current and future climate of North America, *Climate Dynamics*, 49, 71–95, 2017.

709 Lucas-Picher, P., Argüeso, D., Brisson, E., Trambly, Y., Berg, P., Lemonsu, A., Kotlarski, S., and Caillaud, C.: Convection-permitting  
710 modeling with regional climate models: Latest developments and next steps, *Wiley Interdisciplinary Reviews: Climate Change*, 12, e731,  
711 2021.

712 Lucas-Picher, P., Brisson, E., Caillaud, C., Alias, A., Nabat, P., Lemonsu, A., Poncet, N., Cortés Hernandez, V. E., Michau, Y., Doury, A.,  
713 et al.: Evaluation of the convection-permitting regional climate model CNRM-AROME41t1 over Northwestern Europe, *Climate Dynam-*  
714 *ics*, 62, 4587–4615, 2024.

715 Mapes, B., Tulich, S., Lin, J., and Zuidema, P.: The mesoscale convection life cycle: Building block or prototype for large-scale tropical  
716 waves?, *Dynamics of atmospheres and oceans*, 42, 3–29, 2006.

717 Marsham, J. H., Dixon, N. S., Garcia-Carreras, L., Lister, G. M., Parker, D. J., Knippertz, P., and Birch, C. E.: The role of moist convection  
718 in the West African monsoon system: Insights from continental-scale convection-permitting simulations, *Geophysical Research Letters*,  
719 40, 1843–1849, 2013.

720 Merchant, C. J., Embury, O., Bulgin, C. E., Block, T., Corlett, G. K., Fiedler, E., Good, S. A., Mittaz, J., Rayner, N. A., Berry, D., et al.:  
721 Satellite-based time-series of sea-surface temperature since 1981 for climate applications, *Scientific data*, 6, 223, 2019.

722 Miura, H., Satoh, M., Nasuno, T., Noda, A. T., and Oouchi, K.: A Madden-Julian oscillation event realistically simulated by a global cloud-  
723 resolving model, *Science*, 318, 1763–1765, 2007a.

724 Miura, H., Satoh, M., Tomita, H., Noda, A. T., Nasuno, T., and Iga, S.-i.: A short-duration global cloud-resolving simulation with a realistic  
725 land and sea distribution, *Geophysical research letters*, 34, 2007b.

726 Miura, H., Suematsu, T., Kawai, Y., Yamagami, Y., Takasuka, D., Takano, Y., Hung, C.-S., Yamazaki, K., Kodama, C., Kajikawa, Y., et al.:  
727 Asymptotic matching between weather and climate models, *Bulletin of the American Meteorological Society*, 104, E2308–E2315, 2023.

728 Nakamura, Y. and Takayabu, Y. N.: Convective couplings with equatorial Rossby waves and equatorial Kelvin waves. Part I: Coupled wave  
729 structures, *Journal of the Atmospheric Sciences*, 79, 247–262, 2022.

730 Nasuno, T., Tomita, H., Iga, S., Miura, H., and Satoh, M.: Convectively coupled equatorial waves simulated on an aquaplanet in a global  
731 nonhydrostatic experiment, *Journal of the atmospheric sciences*, 65, 1246–1265, 2008.

732 North, R. C., Mittermaier, M. P., and Milton, S. F.: Using SIEPS with a TRMM-derived climatology to assess global NWP precipitation  
733 forecast skill, *Monthly Weather Review*, 150, 135–155, 2022.

734 Ortega, S., Segura, H., Mayta, V. C., Fiévet, R., Bravo, A. P., Lee, J., Giorgetta, M. A., and Stevens, B.: Convectively Coupled Equatorial  
735 Waves in a Global Storm-Resolving Model, *Authorea Preprints*, 2026.

736 Paredes, E. G., Groner, L., Ubbiali, S., Vogt, H., Madonna, A., Mariotti, K., Cruz, F., Benedicic, L., Bianco, M., VandeVondele, J., et al.:  
737 Gt4py: High performance stencils for weather and climate applications using python, *arXiv preprint arXiv:2311.08322*, 2023.

738 Pastorello, G., Trotta, C., Canfora, E., Chu, H., Christianson, D., Cheah, Y.-W., Poindexter, C., Chen, J., Elbashandy, A., Humphrey, M.,  
739 et al.: The FLUXNET2015 dataset and the ONEFlux processing pipeline for eddy covariance data, *Scientific data*, 7, 225, 2020.

740 Perkins-Kirkpatrick, S. and Lewis, S.: Increasing trends in regional heatwaves, *Nature communications*, 11, 3357, 2020.

741 Pichelli, E., Coppola, E., Sobolowski, S., Ban, N., Giorgi, F., Stocchi, P., Alias, A., Belušić, D., Berthou, S., Caillaud, C., et al.: The first multi-  
742 model ensemble of regional climate simulations at kilometer-scale resolution part 2: historical and future simulations of precipitation,  
743 *Climate Dynamics*, 56, 3581–3602, 2021.

744 Pothapakula, P. K., Prein, A. F., Sunkisala, A., and Dipankar, A.: Global Monsoon in ICON: The Scale-Dependent Response of Northern  
745 Hemisphere Monsoons, *EGUsphere*, 2026, 1–41, 2026.

746 Prein, A.: andreas-prein/icon2.5\_dyamond3\_paper: vo.1.0.0, <https://doi.org/10.5281/zenodo.18007290>, 2025.

747 Prein, A. F.: Thunderstorm straight line winds intensify with climate change, *Nature Climate Change*, 13, 1353–1359, 2023.

748 Prein, A. F.: Data used in the publication: From Single Storms to Global Waves: A Global 2.5 km ICON Simulation of Weather and Climate,  
749 <https://doi.org/10.6084/m9.figshare.31341982>, 2026.

750 Prein, A. F. and Gobiet, A.: Impacts of uncertainties in European gridded precipitation observations on regional climate analysis, *International*  
751 *Journal of Climatology*, 37, 305–327, 2017.

752 Prein, A. F., Gobiet, A., Suklitsch, M., Truhetz, H., Awan, N. K., Keuler, K., and Georgievski, G.: Added value of convection permitting  
753 seasonal simulations, *Climate Dynamics*, 41, 2655–2677, 2013.

754 Prein, A. F., Langhans, W., Fossier, G., Ferrone, A., Ban, N., Goergen, K., Keller, M., Tölle, M., Gutjahr, O., Feser, F., et al.: A review on  
755 regional convection-permitting climate modeling: Demonstrations, prospects, and challenges, *Reviews of geophysics*, 53, 323–361, 2015.

756 Prein, A. F., Rasmussen, R. M., Ikeda, K., Liu, C., Clark, M. P., and Holland, G. J.: The future intensification of hourly precipitation extremes,  
757 *Nature climate change*, 7, 48–52, 2017.

758 Prein, A. F., Liu, C., Ikeda, K., Bullock, R., Rasmussen, R. M., Holland, G. J., and Clark, M.: Simulating North American mesoscale  
759 convective systems with a convection-permitting climate model, *Climate Dynamics*, 55, 95–110, 2020.

760 Prein, A. F., Rasmussen, R., Wang, D., and Giangrande, S.: Sensitivity of organized convective storms to model grid spacing in current and  
761 future climates, *Philosophical Transactions of the Royal Society A*, 379, 20190546, 2021.

762 Prein, A. F., Ge, M., Valle, A. R., Wang, D., and Giangrande, S. E.: Towards a unified setup to simulate mid-latitude and tropical mesoscale  
763 convective systems at kilometer-scales, *Earth and Space Science*, 9, e2022EA002295, 2022.

764 Prein, A. F., Ban, N., Ou, T., Tang, J., Sakaguchi, K., Collier, E., Jayanarayanan, S., Li, L., Sobolowski, S., Chen, X., et al.: Towards  
765 ensemble-based kilometer-scale climate simulations over the third pole region, *Climate Dynamics*, 60, 4055–4081, 2023a.

766 Prein, A. F., Mooney, P. A., and Done, J. M.: The multi-scale interactions of atmospheric phenomenon in mean and extreme precipitation,  
767 *Earth's Future*, 11, e2023EF003 534, 2023b.

768 Prein, A. F., Feng, Z., Fiolleau, T., Moon, Z. L., Núñez Ocasio, K. M., Kukulies, J., Roca, R., Varble, A. C., Rehbein, A., Liu, C., et al.:  
769 Km-scale simulations of mesoscale convective systems over South America—A feature tracker intercomparison, *Journal of Geophysical*  
770 *Research: Atmospheres*, 129, e2023JD040 254, 2024.

771 Rackow, T., Pedruzo-Bagazgoitia, X., Becker, T., Milinski, S., Sandu, I., Aguridan, R., Bechtold, P., Beyer, S., Bidlot, J., Boussetta, S., et al.:  
772 Multi-year simulations at kilometre scale with the Integrated Forecasting System coupled to FESOM2. 5 and NEMOv3.4, *Geoscientific*  
773 *Model Development*, 18, 33–69, 2025.

774 Randall, D. A. and Emanuel, K.: The weather–climate schism, *Bulletin of the American Meteorological Society*, 105, E300–E305, 2024.

775 Raschendorfer, M., Simmer, C., and Gross, P.: Parameterisation of turbulent transport in the atmosphere, in: *Dynamics of multiscale earth*  
776 *systems*, pp. 167–185, Springer, 2003.

777 Roberts, M. J., Camp, J., Seddon, J., Vidale, P. L., Hodges, K., Vanniere, B., Mecking, J., Haarsma, R., Bellucci, A., Scoccimarro, E.,  
778 et al.: Impact of model resolution on tropical cyclone simulation using the HighResMIP–PRIMAVERA multimodel ensemble, *Journal of*  
779 *Climate*, 33, 2557–2583, 2020.

780 Sakradzija, M., Senf, F., Scheck, L., Ahlgrimm, M., and Klocke, D.: Local impact of stochastic shallow convection on clouds and precipitation  
781 in the tropical Atlantic, *Monthly Weather Review*, 148, 5041–5062, 2020.

782 Sato, T., Miura, H., Satoh, M., Takayabu, Y. N., and Wang, Y.: Diurnal cycle of precipitation in the tropics simulated in a global cloud-  
783 resolving model, *Journal of Climate*, 22, 4809–4826, 2009.

784 Satoh, M., Matsuno, T., Tomita, H., Miura, H., Nasuno, T., and Iga, S.-I.: Nonhydrostatic icosahedral atmospheric model (NICAM) for global  
785 cloud resolving simulations, *Journal of Computational Physics*, 227, 3486–3514, 2008.

786 Satoh, M., Stevens, B., Judt, F., Khairoutdinov, M., Lin, S.-J., Putman, W. M., and Düben, P.: Global cloud-resolving models, *Current Climate*  
787 *Change Reports*, 5, 172–184, 2019.

788 Savre, J. and Craig, G.: Fitting cumulus cloud size distributions from idealized cloud resolving model simulations, *Journal of Advances in*  
789 *Modeling Earth Systems*, 15, e2022MS003 360, 2023.

790 Schär, C., Leuenberger, D., Fuhrer, O., Lüthi, D., and Girard, C.: A new terrain-following vertical coordinate formulation for atmospheric  
791 prediction models, *Monthly Weather Review*, 130, 2459–2480, 2002.

792 Schär, C., Fuhrer, O., Arteaga, A., Ban, N., Charpiroz, C., Di Girolamo, S., Hentgen, L., Hoefler, T., Lapillonne, X., Leutwyler, D., et al.:  
793 Kilometer-scale climate models: Prospects and challenges, *Bulletin of the American Meteorological Society*, 101, E567–E587, 2020.

794 Schellekens, J., Dutra, E., Martínez-de La Torre, A., Balsamo, G., Van Dijk, A., Sperna Weiland, F., Minvielle, M., Calvet, J.-C., Decharme,  
795 B., Eisner, S., et al.: A global water resources ensemble of hydrological models: the earth2Observe Tier-1 dataset, *Earth System Science*  
796 *Data*, 9, 389–413, <https://doi.org/10.5194/essd-9-389-2017>, 2017.

797 Schenkel, B. A. and Hart, R. E.: An examination of tropical cyclone position, intensity, and intensity life cycle within atmospheric reanalysis  
798 datasets, *Journal of Climate*, 25, 3453–3475, 2012.

799 Schlemmer, L., Schär, C., Lüthi, D., and Strelbel, L.: A groundwater and runoff formulation for weather and climate models, *Journal of*  
800 *Advances in Modeling Earth Systems*, 10, 1809–1832, 2018.

801 Schmidli, J., Böing, S., and Fuhrer, O.: Accuracy of simulated diurnal valley winds in the Swiss Alps: Influence of grid resolution, topography  
802 filtering, and land surface datasets, *Atmosphere*, 9, 196, 2018.

803 Schrodin, R. and Heise, E.: The multi-layer version of the DWD soil model TERRA\_LM, DWD Offenbach, Germany, 2001.

804 Schulz, J.-P. and Vogel, G.: Improving the processes in the land surface scheme TERRA: Bare soil evaporation and skin temperature,  
805 Atmosphere, 11, 513, 2020.

806 Segura, H. and Hohenegger, C.: How do the tropics precipitate? Daily variations in precipitation and cloud distribution, Journal of the  
807 Meteorological Society of Japan. Ser. II, 102, 525–537, 2024.

808 Segura, H., Hohenegger, C., Wengel, C., and Stevens, B.: Learning by doing: Seasonal and diurnal features of tropical precipitation in a  
809 global-coupled storm-resolving model, Geophysical Research Letters, 49, e2022GL101796, 2022.

810 Segura, H., Bayley, C., Fievét, R., Glöckner, H., Günther, M., Kluft, L., Naumann, A., Ortega, S., Praturi, D., Rixen, M., et al.: A single  
811 tropical rainbelt in global storm-resolving models: The role of surface heat fluxes over the warm pool, Journal of Advances in Modeling  
812 Earth Systems, 17, e2024MS004897, 2025a.

813 Segura, H., Pedruzo-Bagazgoitia, X., Weiss, P., Müller, S. K., Rackow, T., Lee, J., Dolores-Tesillos, E., Benedict, I., Aengenheyster, M.,  
814 Aguridan, R., et al.: nextGEMS: entering the era of kilometer-scale Earth system modeling, EGU sphere, 2025, 1–39, 2025b.

815 Seifert, A.: A revised cloud microphysical parameterization for COSMO-LME, COSMO Newsletter 7, Consortium for Small-Scale Mod-  
816 elling, <http://www.cosmo-model.org>, proceedings from the 8th COSMO General Meeting, Bucharest, 2006, 2008.

817 Seneviratne, S. I., Zhang, X., Adnan, M., Badi, W., Dereczynski, C., Luca, A. D., Ghosh, S., Iskandar, I., Kossin, J., Lewis, S., et al.: Weather  
818 and climate extreme events in a changing climate, 2021.

819 Soares, P. M., Careto, J. A., Cardoso, R. M., Goergen, K., Katragkou, E., Sobolowski, S., Coppola, E., Ban, N., Belušić, D., Berthou, S., et al.:  
820 The added value of km-scale simulations to describe temperature over complex orography: the CORDEX FPS-Convection multi-model  
821 ensemble runs over the Alps, Climate Dynamics, 62, 4491–4514, 2024.

822 Song, Y., Broxton, P. D., Ehsani, M. R., and Behrangi, A.: Assessment of snowfall accumulation from satellite and reanalysis products using  
823 SNOTEL observations in Alaska, Remote Sensing, 13, 2922, 2021.

824 Stevens, B., Satoh, M., Auger, L., Biercamp, J., Bretherton, C. S., Chen, X., Düben, P., Judt, F., Khairoutdinov, M., Klocke, D., et al.: DYA-  
825 MOND: the DYNAMICS of the Atmospheric general circulation Modeled On Non-hydrostatic Domains, Progress in Earth and Planetary  
826 Science, 6, 1–17, 2019.

827 Takasuka, D., Kodama, C., Suematsu, T., Ohno, T., Yamada, Y., Seiki, T., Yashiro, H., Nakano, M., Miura, H., Noda, A. T., et al.: How  
828 can we improve the seamless representation of climatological statistics and weather toward reliable global K-scale climate simulations?,  
829 Journal of Advances in Modeling Earth Systems, 16, e2023MS003701, 2024a.

830 Takasuka, D., Satoh, M., Miyakawa, T., Kodama, C., Klocke, D., Stevens, B., Vidale, P. L., and Terai, C. R.: A protocol and analysis of  
831 year-long simulations of global storm-resolving models and beyond, Progress in Earth and Planetary Science, 11, 66, 2024b.

832 Takasuka, D., Becker, T., and Bao, J.: Precipitation characteristics and thermodynamic-convection coupling in global kilometer-scale simu-  
833 lations, Journal of Advances in Modeling Earth Systems, 18, e2025MS005343, 2026.

834 Takayabu, Y. N.: Large-scale cloud disturbances associated with equatorial waves Part I: Spectral features of the cloud disturbances, Journal  
835 of the Meteorological Society of Japan. Ser. II, 72, 433–449, 1994.

836 Taylor, M., Caldwell, P. M., Bertagna, L., Clevenger, C., Donahue, A., Foucar, J., Guba, O., Hillman, B., Keen, N., Krishna, J., et al.: The  
837 simple cloud-resolving E3SM atmosphere model running on the Frontier exascale system, in: Proceedings of the international conference  
838 for high performance computing, networking, storage and analysis, pp. 1–11, 2023.

839 Tomita, H., Miura, H., Iga, S.-i., Nasuno, T., and Satoh, M.: A global cloud-resolving simulation: Preliminary results from an aqua planet  
840 experiment, Geophysical Research Letters, 32, 2005.

841 Trenberth, K. E.: 24.5-Year Surface Radiation Budget Data Set Released, 2011.

842 Virtanen, P., Gommers, R., Oliphant, T. E., Haberland, M., Reddy, T., Cournapeau, D., Burovski, E., Peterson, P., Weckesser, W., Bright, J.,  
843 et al.: SciPy 1.0: fundamental algorithms for scientific computing in Python, *Nature methods*, 17, 261–272, 2020.

844 Weber, N. J. and Mass, C. F.: Subseasonal weather prediction in a global convection-permitting model, *Bulletin of the American Meteorological Society*, 100, 1079–1089, 2019.

846 Weedon, G. P., Balsamo, G., Bellouin, N., Gomes, S., Best, M. J., and Viterbo, P.: The WFDEI meteorological forcing data  
847 set: WATCH Forcing Data methodology applied to ERA-Interim reanalysis data, *Water Resources Research*, 50, 7505–7514,  
848 <https://doi.org/https://doi.org/10.1002/2014WR015638>, 2014.

849 Wheeler, M. and Kiladis, G. N.: Convectively Coupled Equatorial Waves: Analysis of Clouds and Temperature in the  
850 Wavenumber–Frequency Domain, *Journal of the Atmospheric Sciences*, 56, 374 – 399, [https://doi.org/10.1175/1520-0469\(1999\)056<0374:CCEWAO>2.0.CO;2](https://doi.org/10.1175/1520-0469(1999)056<0374:CCEWAO>2.0.CO;2), 1999.

852 World Climate Research Programme: Report of the WCRP km-scale modeling workshop, 3–7 October 2022, hybrid format, Tech. Rep.  
853 08/2022, World Climate Research Programme (WCRP), Geneva, Switzerland, [https://www.wcrp-climate.org/WCRP-publications/2022/WCRP\\_Report\\_08-2022\\_k-scale-report-final.pdf](https://www.wcrp-climate.org/WCRP-publications/2022/WCRP_Report_08-2022_k-scale-report-final.pdf), 2022.

855 Yasunaga, K. and Mapes, B.: Differences between more divergent and more rotational types of convectively coupled equatorial waves. Part  
856 I: Space–time spectral analyses, *Journal of the atmospheric sciences*, 69, 3–16, 2012.

857 Yasunaga, K., Yokoi, S., Inoue, K., and Mapes, B. E.: Space–time spectral analysis of the moist static energy budget equation, *Journal of*  
858 *Climate*, 32, 501–529, 2019.

859 Yu, H., Prein, A. F., Qi, D., and Wang, K.: Mesoscale convective systems in Northeast China from satellite products, global reanalysis, and  
860 kilometer-scale modeling, *Geophysical Research Letters*, 52, e2024GL112 349, 2025.

861 Zängl, G., Reinert, D., Rípodas, P., and Baldauf, M.: The ICON (ICOsahedral Non-hydrostatic) modelling framework of DWD and MPI-M:  
862 Description of the non-hydrostatic dynamical core, *Quarterly Journal of the Royal Meteorological Society*, 141, 563–579, 2015.

863 Zhang, Z., Varble, A. C., Feng, Z., Marquis, J. N., Hardin, J. C., and Zipser, E. J.: Dependencies of simulated convective cell and system  
864 growth biases on atmospheric instability and model resolution, *Journal of Geophysical Research: Atmospheres*, 129, e2024JD041 090,  
865 2024.